Research papers

Dependence of tides and river water transport in an estuarine network on river discharge, tidal forcing, geometry and sea level rise

Jinyang Wang [a,*], Huib E. de Swart [a], Yoeri M. Dijkstra [b]

[a] *Institute for Marine and Atmospheric research Utrecht (IMAU), Utrecht University, Utrecht, The Netherlands*
[b] *Delft Institute of Applied Mathematics, Delft University of Technology, Delft, The Netherlands*

ARTICLE INFO

ABSTRACT

Estuaries are often characterised by a complex network of branching channels, in which the water motion is primarily driven by tides and fresh water discharge. For both scientific reasons and management purposes, it is important to gain more fundamental knowledge about the hydrodynamics in such networks, as well as their implications for turbidity and ecological functioning. A generic 2DV estuarine network model is developed to study tides and river water transport and to understand the dependence of their along-channel and vertical structure on forcings, geometry characteristics and sea level changes. The model is subsequently applied to the Yangtze Estuary to investigate tides and the distribution of river water over channels during dry and wet season, spring tide, as well as prior to and after the formation of Hengsha Passage and the construction of the Deep Waterway Project and sea level rise. Increasing river discharge enhances the friction for tides by increasing both internal and bottom stresses. Changes in tidal forcing are correlated with the friction for both tide and river. A shortcut channel reduces the water level difference in adjacent channels, as well as tidal amplitudes difference. Sea level rise results in larger friction parameters and faster propagation of tides. The distribution of river water transport is hardly affected by above mentioned changes. Model results and current vertical structure are consistent with observations.

1. Introduction

Many of the world's estuaries have the structure of a network with multiple connected channels. Examples are the Yangtze Estuary (China), the Mahakam Delta (Indonesia), the Pearl River Delta (China) and the Berau Estuary (Indonesia). Compared to a single-channel estuary, the network structure adds further complexity to the dynamics. Knowledge of the tides and transport of river water of estuarine networks is important to prevent coastal flooding, manage fresh water supply and for ecology (transport of matter, turbidity dynamics, etc.) This is especially important since human interventions (e.g. dredging and constructions) and climate change (e.g. sea level rise) may strongly alter the conditions of the entire system (Winterwerp et al., 2013; Cheng et al., 2018).

Besides focusing on the water levels alone, accounting for the vertical structure of tidal currents is considered to be important, as velocity shear is crucial for e.g. sediment dynamics and ecology (Cloern et al., 2016; Dijkstra et al., 2019). In this study, we focus on the vertical structure of tidal and river flows in networks from the perspective of an idealised model. An idealised model is a useful tool, because it can help to reveal the contribution of individual physical processes. Moreover, such a model is fast and therefore suitable for sensitivity studies.

Tidal propagation in a single channel estuary has been investigated by numerous researchers (Friedrichs, 2010; Geyer and MacCready, 2014; Talke and Jay, 2020, and references therein). The evolution of water level and tidal discharge is well understood in terms of analytical relations and sensitivity to changing parameters (Friedrichs and Aubrey, 1988, 1994; Ridderinkhof et al., 2014; Lanzoni and Seminara, 1998). Also the vertical structure of tidal current has been studied (Ianniello, 1977, 1979). Numerical models exist to simulate tidal dynamics in networks. E.g. Buschman et al. (2010) used an idealised 2DH numerical model to examine the effect of amplitude of M_2 sea surface elevations on the division of river water transport at the delta apex junction in the Berau region. Sassi et al. (2011) used a numerical 2DH model to show that, in the east part of Mahakam Delta, Indonesia, a so-called differential water level setup occurred. This concerns the modification of river discharge distribution over channels due to subtidal water level difference that arises from the interaction of surface elevations induced by subtidal flow and river. Full 3D numerical models of Zhu et al. (2018) for the Yangtze Estuary successfully simulated tides and net water transport prior to and after a major intervention, the Deep Waterway Project (DWP) that comprised

---

the deepening and narrowing of one channel of this estuarine network. However, the more fundamental understanding of tidal propagation in estuarine networks in terms of analytical solutions and parameters sensitivities is less well-developed. Tides in a channel network were first studied by Lorentz (1926). He developed an 1D (cross-sectional averaged) analytical model to quantify tides and storm surges in the Dutch Wadden Sea and Zuiderzee prior to and after the construction of a dyke. A generic analytical linear 1D network model for tides was developed by Hill and Souza (2006). They applied it to investigate tides in a fjord system in east of Queen Charlotte Sound, western Canada, where friction is weak. Alebregtse and de Swart (2016) extended the Hill and Souza (2006) model such that it also describes nonlinear tides and net water transport in friction-dominated estuaries and applied their model to the Yangtze Estuary.

However, idealised models for tidal dynamics in networks resolving the vertical current structure are missing. Hence, the first aim of this study is to develop a vertically resolving idealised model for tides and river discharge in estuarine networks. The second aim is to use this model to gain more fundamental understanding of tides and transport of river water in a network and how this responds to changes in river discharge, tidal forcing, geometry, and sea level rise. Specifically, this work adds the interaction between eddy viscosity, bottom friction and tidal propagation in a network under several local and global modifications.

The 2DV network model will be used to examine the Yangtze Estuary (YE), which is characterised by strong seasonal cycles in both river discharge and tidal forcing (Guo et al., 2015). In addition, multiple changes in geometry occurred in this estuary over last century due to both anthropogenic activities and natural evolutions. Besides the already mentioned DWP, a shortcut channel, the Hengsha Passage (HP), formed during the severe floods in 1954 and thereby enriched the branching characteristics of the YE (Kuang et al., 2014a). Furthermore, the YE is subject to sea level rise (SLR) (Kuang et al., 2017), which increases the difficulty for decision makers to implement adequate management strategies (Cheng et al., 2018).

This manuscript is organised as follows. Section 2 describes the model geometry and outlines the derivation of the final equations that govern the tide–river system. Section 3 presents the results from applying the model to the Yangtze Estuary, with focus on the effects of changes in the forcings and geometry on tidal characteristics (i.e., amplitudes and phases of tidal currents and surface elevations) and the magnitudes of river water transport. Section 4 contains the discussion, followed by the conclusion in Section 5.

2. Model and methods

2.1. Model

2.1.1. Domain

Consider an idealised estuarine network system that consists of multiple connected channels. The water motion is forced by both river discharge at the various river heads and by tidal sea surface variations. Each channel has a constant depth H_j and a constant length L_j, where j is the channel index. Cartesian coordinates x and z are used, where the positive x-direction is seaward and the z-axis points vertically upwards, with $z = 0$ the approximate subtidal water level, which is assumed to be constant for each channel. The width b_j of each channel is assumed to vary exponentially in x and does not depend on z, i.e.,

$$b_j(x) = b(L_j)\exp\left(\frac{x - L_j}{l_{b,j}}\right), \qquad 0 \le x \le L_j. \tag{1}$$

In this expression, $l_{b,j}$ is the length scale at which channel width increases exponentially in the seaward direction. Channel labelling is explained in Fig. 1. Channel index will be omitted from hereon for simplicity if the equations hold for all channels, unless specified otherwise.

2.1.2. Equations of motion

The equations governing tides and river water transport are the width-averaged shallow water equations. It is assumed that advection, horizontal dispersion, drying/flooding of tidal flats, and the baroclinic pressure gradient are negligible. Next, the water motion, to the leading order, is assumed to consist only of M_2 and subtidal component. The resulting equations at each frequency are (see e.g. Ianniello, 1979)

$$\frac{\partial u_n}{\partial t} = -g\frac{\partial \eta_n}{\partial x} + \check{A}_{vn}\frac{\partial^2 u_n}{\partial z^2}, \tag{2a}$$

$$\frac{\partial u_n}{\partial x} + \frac{\partial w_n}{\partial z} + \frac{1}{l_b}u_n = 0. \tag{2b}$$

Here, the subscript n denotes the harmonic component (0 for subtidal and 1 for M_2 tide), u and w are the horizontal and vertical width-averaged velocities, respectively. Furthermore, η is the free surface elevation with respect to the undisturbed water level $z = 0$, g is the gravitational acceleration and $\check{A}_{vn}$ is a constant vertical eddy viscosity coefficient, to be determined, which has a different value for subtidal ($n = 0$) and M_2 ($n = 1$) motion. Using a depth-uniform constant eddy viscosity is most applicable for partially to well-mixed estuaries, not strongly stratified ones. The boundary conditions for each harmonic read

$$\check{A}_{vn}\frac{\partial u_n}{\partial z} = 0 \quad \text{and} \quad w_n = \frac{\partial \eta_n}{\partial t} \qquad \text{at} \quad z = 0, \tag{3a}$$

$$\check{A}_{vn}\frac{\partial u_n}{\partial z} = \check{s}_{fn}u_n \quad \text{and} \quad w_n = 0 \qquad \text{at} \quad z = -H, \tag{3b}$$

where $\check{s}_{fn}$ is the slip parameter, which, like $\check{A}_{vn}$ is different for the subtidal and M_2 motion, to be determined. It is assumed that there is no wind stress at the free surface and a linearised kinematic boundary condition is applied (Eq. (3a)). The condition for this linearisation to be valid is that the sea surface amplitudes are much smaller than the mean depth (Chernetsky et al., 2010). The partial slip bottom boundary condition is used (Eq. (3b)) (Maas and van Haren, 1987; Schramkowski and de Swart, 2002).

Tidal sea surface elevations with a single angular frequency ω are prescribed at all seaward boundaries and a constant fresh water discharge Q is assumed at the tidal limit. At each branching point, the actual level of the sea surface η is assumed to be continuous and the fluid obeys mass conservation. This results in

$$\eta_{n,j} = \delta_{n1}Z_j\cos\left(\omega t - \phi_j\right), \qquad \text{at } x = L_j \text{ for sea channels}, \tag{4a}$$

$$b_j\int_{-H_j}^0 u_{n,j}\mathrm{d}z = \delta_{n0}Q_j, \qquad \text{at } x = 0 \text{ for river channels}, \tag{4b}$$

$$\eta_{n,j} = \eta_{n,k}, \qquad \text{at branching points } v_i, \quad j,k \in v_i, \tag{4c}$$

$$\sum_{j\in I_i} b_j\int_{-H_j}^0 u_{n,j}\mathrm{d}z = \sum_{j\in O_i} b_j\int_{-H_j}^0 u_{n,j}\mathrm{d}z, \quad \text{at branching points } v_i, \quad j\in v_i, \tag{4d}$$

with Z_j and ϕ_j are the prescribed tidal amplitude and phase at the sea boundaries. Eqs. (4c) and (4d) mean that at the branching points sea level is continuous and mass is conserved. Here, v_i is a set of indices of channels that connect at branching point i. The index set v_i is further decomposed into I_i and O_i, which respectively contain indices of channels in which the fluid flows towards or away from branching point v_i. A specific example of this network labelling is given in Fig. 1.

2.2. Turbulence model

The values of effective eddy viscosities and slip parameters are realistically different for each harmonic component n (e.g. Godin, 1991, 1999). To determine these, it is assumed that the total energy dissipation in each harmonic component is the same as when using a space- and time-dependent turbulence closure. Hence this method may
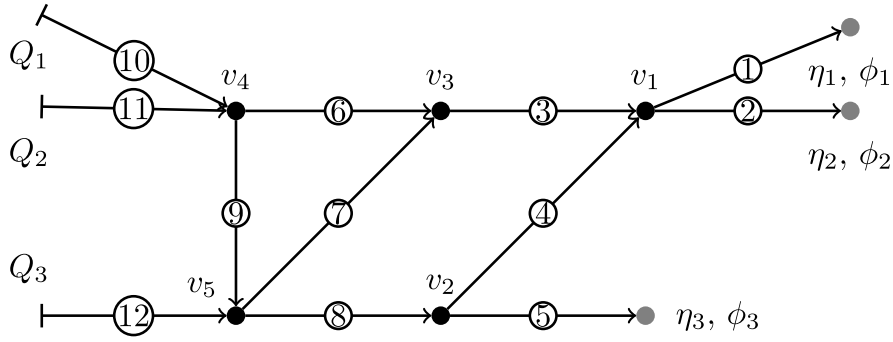
Fig. 1. A schematic diagram for an arbitrary estuarine network, following Hill and Souza (2006). Channel indices are in white circles. Solid grey circles denote open sea with tidal forcings indicated next to them. Channels connected to the sea are referred to as sea channels. The closed ends (tidal limit or a weir) of so-called river channels are shown as vertical bars; at these locations a constant river discharge is prescribed and the tidal current vanishes. The set of indices for each branching point is denoted by v_i. Here, $v_1 = \{-1, -2, 3, 4\}$, $v_2 = \{-4, -5, 8\}$, $v_3 = \{-3, 6, 7\}$, $v_4 = \{-6, -9, 10, 11\}$, $v_5 = \{-7, -8, 9, 12\}$, where the numbers between braces denote the channels that are connected at each branching point. Positive and negative signs indicate whether the positive x-direction of that channel is pointing towards or away from the branching point.

be regarded as a width-averaged extension of the Lorentz linearisation method (Lorentz, 1926; Zimmerman, 1982). Denote the averaging over channel and one tidal cycle by an overline, the mean energy dissipation due to the last term in the momentum equation Eq. (2a) is

$$\check{D}_n = \check{A}_{vn} \left(\frac{1}{HLT} \int_0^T \int_{-H}^0 \int_0^L \left(\frac{\partial u_n}{\partial z} \right)^2 \mathrm{d}x \, \mathrm{d}z \, \mathrm{d}t \right) = \check{A}_{vn} \overline{\left(\frac{\partial u_n}{\partial z} \right)^2}, \quad (5)$$

where T is the period of one tidal cycle. In the model, stresses have been related to constants $\check{A}_{vn}$ and $\check{s}_{fn}$, whereas in reality these parameters depend on space and time. Therefore, eddy viscosity in the space- and time-dependent turbulence model is parameterised by the Prandtl mixing length hypothesis (Bradshaw, 1974)

$$A_v(x, z, t) = l^2 \left| \frac{\partial u}{\partial z} \right|. \quad (6)$$

Here, u is the local velocity that depends on both space and time, l is the mixing length, which is usually assumed to be proportional to the distance to the wall for a wall-bounded flow (Kundu et al., 2016). In this study, a parabolic profile is assumed (for a detailed discussion of this profile see Chen and de Swart (2016))

$$l = \begin{cases} (\zeta + 1) \left(\frac{\zeta_h}{2+\zeta_h} - \zeta \right) H, & -1 \le \zeta \le \zeta_h, \\ (\zeta_h + 1) \left(\frac{\zeta_h}{2+\zeta_h} - \zeta_h \right) \left(\frac{\zeta}{\zeta_h} \right)^2 H, & \zeta_h < \zeta \le 0, \end{cases} \quad (7)$$

where $\zeta = \frac{z}{H}$ is the scaled depth and ζ_h is an input parameter that indicates the location of the boundary between the upper and the lower layer. The value of ζ_h is near the depth at which the eddy viscosity attains the maximum. Note that Eq. (7) only parametrically accounts for the effects of stratification on turbulence through calibration of ζ_h.

The local kinematic internal stress is

$$\tau = A_v \frac{\partial u}{\partial z}. \quad (8)$$

A harmonic truncation is applied to the local kinematic internal stress so that it is decomposed into different harmonic components (for details see Appendix A),

$$\tau = \tau_0(x, z) + \tau_1(x, z, t). \quad (9)$$

The mean energy dissipation attained by the space- and time-dependent turbulence closure is therefore $D_n = \overline{\tau_n \frac{\partial u_n}{\partial z}}$. This is required to equal $\check{D}_n$ (Eq. (5)). Hence $\check{A}_{vn}$ is determined as

$$\check{A}_{vn} = \frac{\overline{\tau_n \frac{\partial u_n}{\partial z}}}{\overline{\left(\frac{\partial u_n}{\partial z} \right)^2}}. \quad (10)$$

The mean energy dissipation at the bottom due to the boundary condition in Eq. (3b) is

$$\check{D}_{bn} = \check{s}_{fn} \left(\overline{u_{bn}} \right)^2, \quad (11)$$

where u_b is the local bottom velocity. In the space- and time-dependent turbulence closure, the bottom slip parameter is modelled by

$$s_f = C_{100} |u_b|, \quad (12)$$

where C_{100} is a drag coefficient that depends on the bottom type. The local bottom stress is also decomposed into different harmonic components

$$\tau_b = s_f u_b = \tau_{b0}(x) + \tau_{b1}(x, t). \quad (13)$$

The corresponding mean energy dissipation is therefore $D_{bn} = \overline{\tau_{bn} u_{bn}}$. This is required to equal $\check{D}_{bn}$. Hence, the constant slip parameters are determined as

$$\check{s}_{fn} = \frac{\overline{\tau_{bn} u_{bn}}}{\overline{u_{bn}^2}}. \quad (14)$$

In this study, both eddy viscosities and slip parameters are called friction parameters that are related to internal and bottom frictions. The internal friction is $\frac{\partial \tau}{\partial z}$ and its mean value is the same as the mean value of last term in Eq. (2a) because of the turbulence model. Whereas the bottom friction is defined as $\frac{\tau_b}{H}$, which is the stress that is experienced by the depth-averaged current.

2.3. Definition of river water transport

It follows, from integration of the continuity equation for the river flow over depth and application of the boundary conditions $w_0 = 0$ at $z = 0$ and $z = -H$, that

$$\frac{\partial}{\partial x} \left[b_j(x) \int_{-H_j}^0 u_{0,j} \, \mathrm{d}z \right] = 0. \quad (15)$$

The quantity between the square brackets is therefore a constant in each channel and defined to be the river water transport Q_j of each channel. The values of Q_j are determined by the conditions at the branching points.
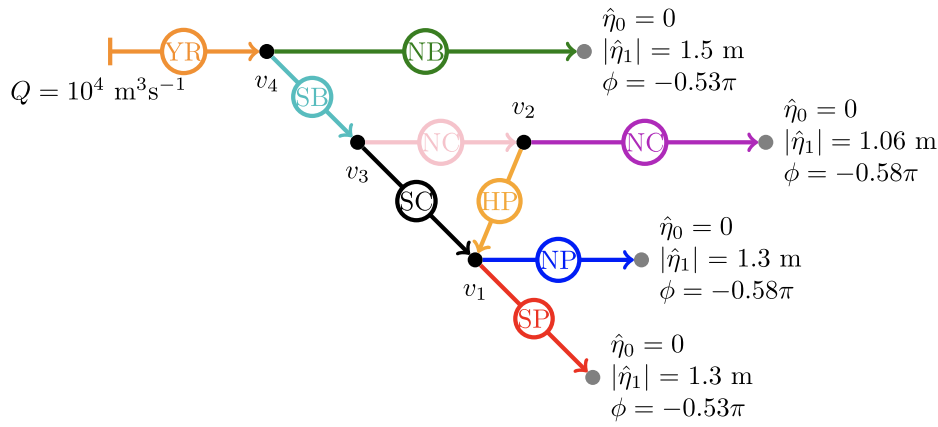
Fig. 2. The network diagram for the Yangtze Estuary. Notations are explained in Fig. 1. Colour coding of channels is the same as that in subsequent plots for easy identification. In the absence of the shortcut channel, the HP is not considered. Forcing conditions are those applied to the reference case, with the shortcut channel being present.

2.4. Model solutions

The solutions of system (2)–(4) are derived in Appendix B. Those for river flow read (for each channel)

$$u_0(x,z) = \frac{gH^2}{\check{A}_{v0}} \left[\frac{1}{2} \left(\zeta^2 - 1 \right) - r \right] \frac{d\eta_0}{dx} = \frac{Q}{b(x)H} \left(\frac{1}{\frac{1}{3} + r} \right) \left[\frac{1}{2} \left(1 - \zeta^2 \right) + r \right],$$

(16a)

$$\frac{d\eta_0}{dx} = -\frac{Q \check{A}_{v0}}{gb(x)H^3 \left(\frac{1}{3} + r \right)},$$

(16b)

where $r^{-1} = \frac{H \check{s}_{f0}}{\check{A}_{v0}}$ is a dimensionless slip parameter. In each channel, the constant river water transport Q (except for river channels in which river discharge is prescribed) and the elevation at the beginning point of the channel, are determined by the boundary conditions (Eq. (4b)).

The solutions for the tidal flow velocities and elevation are

$$(u_1, w_1) = \text{Re}\{(\hat{u}_1, \hat{w}_1)e^{-i\omega t}\}, \quad \eta_1 = \text{Re}\{\hat{\eta}_1 e^{-i\omega t}\},$$

(17)

where a hat denotes the complex amplitude that determines the spatial structure of each variable. The variables $\hat{u}_1$, $\hat{w}_1$ are functions of x and z and $\hat{\eta}_1$ depends only on x. The expressions for the complex amplitudes read

$$\hat{u}_1 = -\frac{ig}{\omega} \left[1 - \beta \cosh(\gamma z) \right] \frac{d\hat{\eta}_1}{dx},$$

(18a)

$$\hat{w}_1 = \frac{ig}{\omega} \left[z - \frac{\beta}{\gamma} \sinh(\gamma z) \right] \left(\frac{d^2\hat{\eta}_1}{dx^2} + \frac{1}{l_b} \frac{d\hat{\eta}_1}{dx} \right) - i\omega\hat{\eta}_1,$$

(18b)

$$\hat{\eta}_1 = e^{-\frac{1}{2l_b}x} \left(C_1 e^{d_0 x} + C_2 e^{-d_0 x} \right),$$

(18c)

with

$$\beta = \frac{1}{\cosh(\gamma H) + \frac{\check{A}_{v1}}{\check{s}_{f1}} \gamma \sinh(\gamma H)} \quad \text{and} \quad \gamma = \sqrt{-\frac{i\omega}{\check{A}_{v1}}}.$$

(19)

Note that $|\gamma|^{-1}$ is the Stokes depth that describes the height of frictional influence (Souza, 2013). The integration constants C_1 and C_2 are determined by the boundary conditions. The complex wave number d_0 is given by

$$d_0 = \sqrt{\left(\frac{1}{2l_b} \right)^2 - \frac{\omega^2}{gH \left(1 - \frac{\beta \sinh(\gamma H)}{\gamma H} \right)}}.$$

(20)

There are two unknown constants in both river (η_0 and Q) and tidal flows (C_1 and C_2). For each flow component, all unknown constants

Table 1
Geometry of the reference Yangtze Estuary network, including the channel length L, the length scale l_b at which channel width increases exponentially in the seaward direction, the water depth H and the width at the seaward boundary b_o.

Channel	Label	L (km)	l_b (km)	H (m)	b_o (km)
North Branch (NB)	1	85	30	5	12
North Channel (NC)	2	60	52	7	20
North Passage (NP)	3	61	470	11	3.5
South Passage (SP)	4	54	21	7	30
South Channel (SC)	5	23	−368	9	6.2
South Branch (SB)	6	51	64	9	14
Yangtze River 1 (YR1)	7	50	206	10	6.6
Yangtze River 2 (YR2)	8	50	206	10	5.2
Yangtze River 3 (YR3)	9	50	206	10	4.1
Yangtze River 4 (YR4)	10	50	206	10	3.2
Yangtze River 5 (YR5)	11	370	206	10	2.5

are solved simultaneously with the boundary and matching conditions (Eq. (4)). Values for eddy viscosity and slip parameter of both river and tidal flow are obtained iteratively. Starting from an initial guess of their values, solutions are calculated, which yield u_0 and u_1. New estimates of $\check{A}_{vn}$ and $\check{s}_{fn}$ are then determined from Eqs. (10) and (14). Then the values of the friction parameters are computed again until changes in these values are less than a user-specified tolerance (here 10^{-5}). The full solution procedure is summarised using a flow chart (see Appendix C).

2.5. Application to the Yangtze Estuary

The Yangtze Estuary is an estuarine network that connects the Yangtze river, also known as the Chang Jiang, with the East China Sea. Prodigious natural variability can be observed in both the river and the sea. The monthly averaged Yangtze river discharge varies from 10^4 m³/s (during the dry season, May to October) to 4×10^4 m³/s (during the wet season, November to April) with an annual average of $28\,300$ m³/s (Yang et al., 2015). During spring tide, the tidal range at the entrance is about 4.62 m, while the average tidal range is 2.67 m (Zhang et al., 2016). Due to large scale human interventions, such as the DWP in the North Passage and the construction of Qingcaosha Freshwater Reservoir, both tidal currents and the distribution of river water over different channels changed.

The default case that is considered in this study is the dry season (January, 2014), during mean tide, after the construction of the DWP and without the Hengsha Passage. The only external tide is the semi-diurnal tide with angular frequency $\omega = 1.4 \times 10^{-4}$ rad/s. Fig. 2 shows the network pattern of the Yangtze Estuary and indicates the values

Table 2
List of experiments.

	Description	Changes
1	Reference	Dry season, monthly-averaged tidal forcing
2	Wet season	River discharge $Q = 4 \times 10^4$ m^3/s (Alebregtse and de Swart, 2016) Increase water depths in YR1–YR5 by 1–5 m respectively (Cai et al., 2019)
3	Spring tide	Increase the tidal amplitudes by 50% (Lu et al., 2015)
4	Shortcut channel	Add Hengsha passage (Kuang et al., 2014a)
5	Before DWP	$H = 7$ m and $l_b = 60$ km in the North passage (Alebregtse and de Swart, 2016)
6	Sea level rise	Undisturbed water depth +2 m (Kuang et al., 2017)

Table 3
Tidal stations of which data have been used to verify the model.

	Station name		Station name		Station name
1	Jiangyin	6	Nanmengang	11	Beicaozhong
2	Tianshengang	7	Shidongkou	12	Niupijiao
3	Hupu	8	Wusong	13	Zhongjun
4	Baimaokou	9	Changxing	14	Nancaodong
5	Qinglonggang	10	Hengsha	15	Sheshan

of the forcing parameters. The parameters for all channels are given in Table 1. The modelled tides from the reference case will be first compared with the observed tides. Next, several scenarios that mimic wet season, spring/neap tide, a shortcut channel, the situation before DWP and sea level rise will be compared to the reference case to investigate their effects on tides, river and river water transport. Table 2 provides the list of experiments. Finally, for all cases, the bottom drag coefficient is $C_{100} = 0.0022$ corresponding to muddy beds (Soulsby, 1997). By fitting the modelled tidal elevation amplitudes to observed amplitudes, it was found that $\zeta_h = -0.67$, meaning that the eddy viscosity is maximum near $-0.67H$ for all channels and thereby also determines the magnitude of the eddy viscosity.

3. Results

3.1. Reference case

Fig. 3 shows the friction parameters of each channel for the reference case. Water depth of each channel is attached to each channel in panel (a). Although the formulation of eddy viscosity (Eqs. (6)–(7)) scales with both depth and velocity, the magnitudes of eddy viscosities turns out to be characterised mostly by the water depths. The eddy viscosities for the river and tidal flow (panel a and b) are therefore the largest in the North Passage (NP, the deepest branch) and the smallest in the North Branch (NB, the shallowest branch).

The slip parameters for the river and tidal flow (panel c and d) are the largest in the North Branch (NB) and the smallest in the South Branch (SB).

Fig. 4(a) and (b) compare the amplitudes and phases of M$_2$ sea surface elevations of the reference case with those derived from harmonic analysis of observed sea surface variations. Dots are data from National Marine Data and Information Service (2013), retrieved from tidal tables for January 2014 of 15 different water stations listed in Table 3. These are the values used to calibrate the model. Upward triangles show results from Lu et al. (2015), who applied harmonic analysis to observed water levels. There is good agreement between modelled and observed tides (see also data presented in Guo et al. (2015), which is plotted in Alebregtse and de Swart (2016)). The tidal damping and amplification in the North Branch (NB) and the South Branch (SB) agree with the result in Zhang et al. (2012): in the NB, tidal wave is first amplified and then damped, whereas in the SB, the tidal wave is damped. The slopes of phase curves in panel (b) are proportional to the phase speed ($c = \omega / \frac{d\phi}{dx}$) of the tidal wave. Typical values of the phase speed, depending on the water depth and on the values of

the friction parameters, range from 7 to 10 m/s. Depth-averaged tidal (M$_2$) current amplitudes (panel c) are almost identical to those from the 1D model of Alebregtse and de Swart (2016). The amplifications in both the North Branch (NB) and the South Passage (SP) are due to the strong width convergence. The amplification in the SP is also observed by Li et al. (2018). For all channels, the surface elevations due to the river flow (panel d) and due to resonance related to wave reflection decrease from river to sea. For most channels, the river flow velocities (panel e) exponentially decrease in magnitude towards sea due to the seaward increasing channel width. The width of the South Channel decreases in the seaward direction and therefore the river flow is amplified in that channel. The North Passage has a nearly constant width (large value of parameter l_b), so that the river current is almost a constant. River water is mostly transported through the South Branch (panel f), after which the river water is distributed nearly evenly over subsequent channels. Percentages next to the lines indicate the river water diversion ratio, computed by the model. It is defined as the ratio of river water transport in one channel to the river water transport in its upstream channel. It should be noted that the river water diversion ratio is different from the net water diversion ratio as in e.g. Alebregtse and de Swart (2016), which additionally includes the net transport due to tides and nonlinear processes and is therefore comparable to the observed water diversion.

The vertical distribution of tidal velocity amplitude (Fig. 5) reveals that tidal current is the strongest near the surface, values can be up to 1.8 m/s. Both the vertical and the horizontal structure of the tidal current amplitudes differ from channel to channel. Viewing upstream, modelled tidal current amplitude decreases in the North Passage and the South Channel, while it increases in the South Passage. These results agree with the results of other analytical studies (Jiang et al., 2013; Alebregtse and de Swart, 2016), while observations suggest more smaller scale longitudinal perturbations due to the complex geometry (Shao et al., 2017). The horizontal variation in the South Passage is much larger than that in the other two channels. At the branching point, there is a jump in tidal velocity amplitude; the tidal current amplitude in the South Passage is about twice as large as those of the North Passage and the South Channel. The large tidal current in the South Passage near the branching point is the result of its strong longitudinal width convergence. However, its width and depth are the smallest among the three channels that join at the branching point, so it has the least cross-section area. This in turn leads to the jump in the velocity at the junction of the NP, the SP and the SC.

3.2. Comparison of wet season with dry season

During the wet season (river discharge is four times higher than that in the dry season), the water level set-up in the Yangtze River (YR) is significant and should be accounted for in order to get correctly simulated tidal propagation (see also Dijkstra et al., 2017) Therefore depths of the YR1 to the YR5 are increased by $1 - 5$ metres respectively. These depth modifications are based on the observed variations in the mean water level in relation to the river discharge (Guo et al., 2015; Cai et al., 2019). Note that although the increase in water depth is not
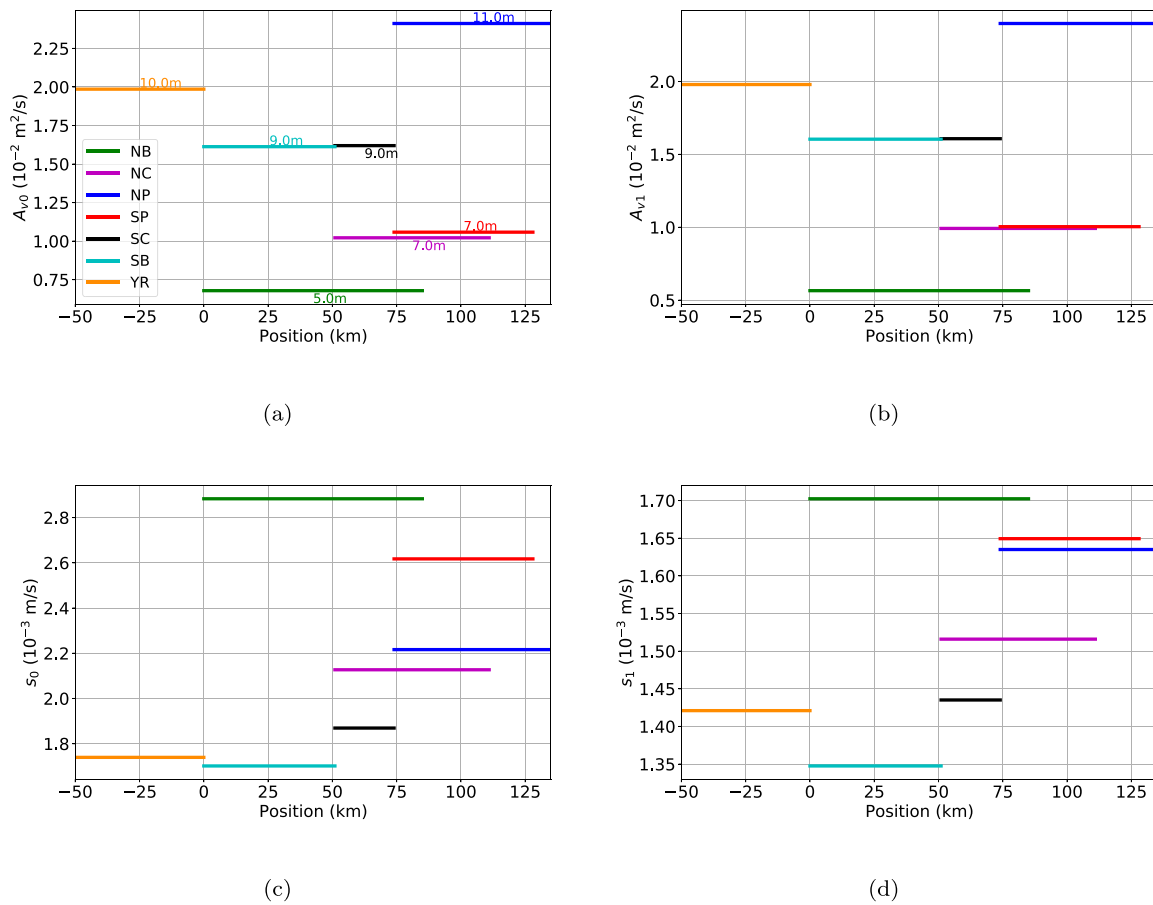
Fig. 3. a. Eddy viscosity A_{v0} of river flow versus position in the network. Here, $x = 0$ is the location of the most upstream branching point. b. As a, but for eddy viscosity A_{v1} of tidal flow. c. As a, but for slip parameter s_0 of river flow. d. As c, but for slip parameter s_1 of tidal flow.

continuous, free surface is guaranteed to be continuous by the matching condition (Eq. (4c)).

The relative changes in friction parameters during the wet season with respect to the dry season are shown in Fig. 6. With larger river discharge, the friction parameters for both river and tide increase, except for the slip parameter of the river flow in the North Branch (NB). This influence decreases downstream and is much smaller on the slip parameter for the river flow. The increase in friction parameters is mostly because of the stronger river–tide interaction due to larger river current, as the influence of larger discharge on water depth is negligible in the downstream part of the Yangtze Estuary.

Fig. 7 shows that the amplitudes of both tidal surface elevations and depth-averaged tidal currents (panel a and c) are smaller in the wet season than in the dry season and the overall dampening increases upstream. This result is consistent with that of Alebregtse and de Swart (2016). Positive phase differences (panel b) in the tidal surface elevations imply that the tidal waves travel slower during the wet season. Under the same tidal forcing, high water arrives at the first branching point about 13 minutes later ($1\,\mathrm{rad} \approx 7114\,\mathrm{s}$). The differences between the horizontal tidal velocity amplitudes during the wet and dry season for longitudinal sections in the South Channel, the North Passage and the South Passage are plotted in panels d, e and f. To make variables comparable between two scenarios at different depths in the cases that channel depths are adjusted, the ζ-coordinate ($\zeta = \frac{z}{H}$) is used instead of the z-coordinate in the difference plots. Here, the water depths in the SC, the NP and the SP are the same for both dry and wet seasons. Solid lines are levels with positive values and dashed lines are levels with negative values. Horizontal tidal velocity amplitudes are generally

smaller during the wet season. At the sea boundaries of the North Passage and the South Passage, these amplitudes are hardly affected by the larger river discharge. For most locations, the change in tidal current amplitude at the surface is larger than that at the bottom.

Plots of the difference between the elevation and current due to the river, as well as the river water transport during the wet season and the dry season are shown in Fig. 1 of the supplementary information (SI). It appears that the spatial patterns of these variables during the wet season are similar as those during the dry season, but larger magnitudes.

SI Fig. 2 shows the sensitivity of selected variables to continuous change in the river discharge from the YR. As river discharge increases, tidal elevation amplitudes (panel a) decrease at all branching point and the time tidal waves need to travel to the branching points (panel b) increases. River set-up (panel c) at all branching points and river water transport (panel d) in each channel linearly increase when the river discharge from the YR is increased.

3.3. Comparison of spring tide with mean tide

By seeing the M_2 tide as a representative semi-diurnal amplitude, spring tide may be considered by increasing the amplitude of the M_2 tide to the amplitude of the semi-diurnal water motion a few days around the spring tide. This approach follows what is used in other studies (Valle-Levinson et al., 2000; Geyer and MacCready, 2014). During spring tide (external tidal amplitude is 50% larger than the mean tide), all friction parameters have larger values. For each channel, the relative changes of friction parameters for the river flow are larger
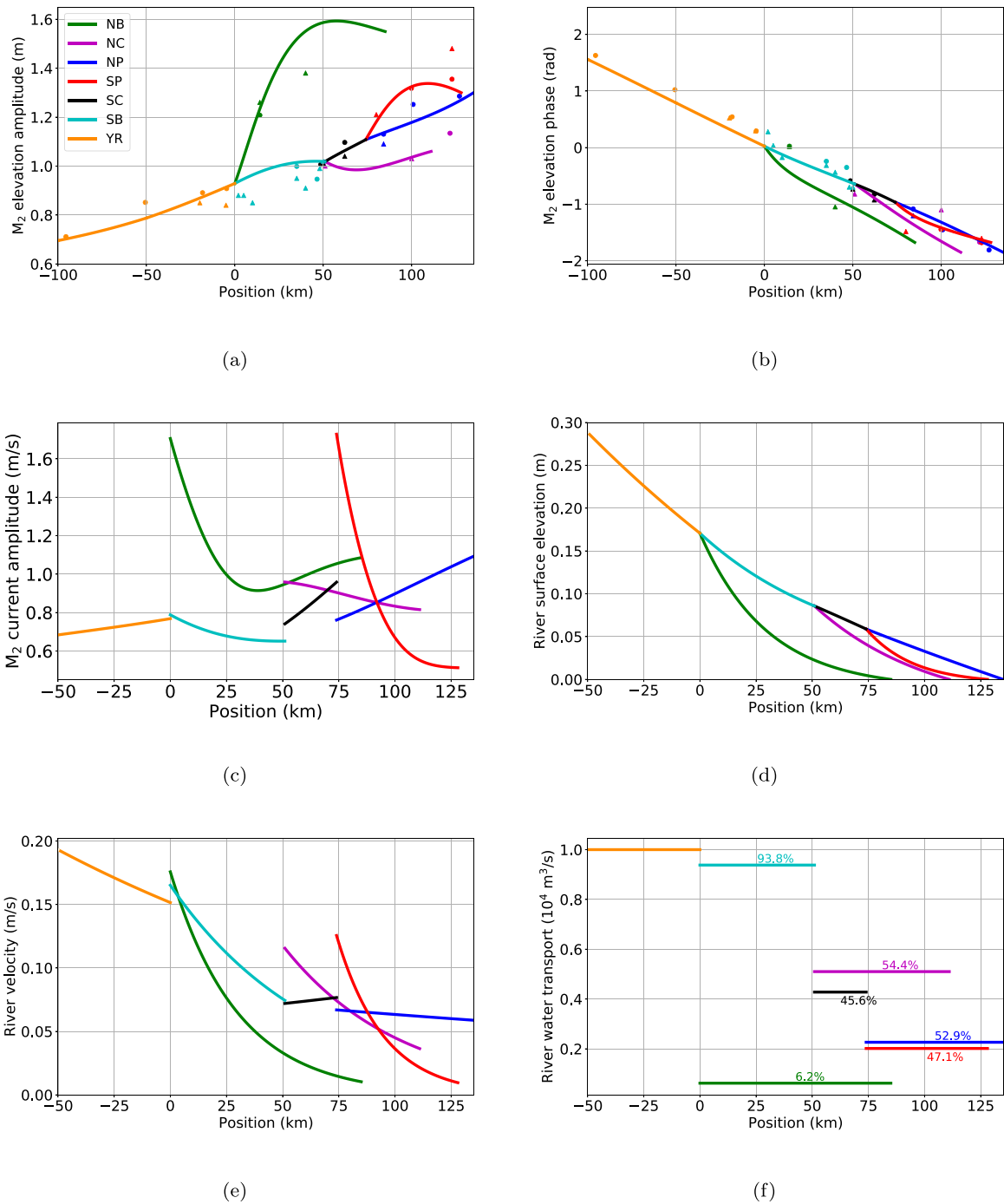
Fig. 4. a. M$_2$ tidal elevation amplitude versus position in the network of the reference case. Here, solid lines are the model results and dots are the data from tidal table. b. As a, but for tidal elevation phase. c. As a, but for tidal discharge amplitudes. d. As a, but for surface elevation due to the river flow. e. As a, but for river flow velocity. f. As a, but for river water transport. Note that x-coordinate for panel a and b is different due to the location of the data point near x = −100 km.

than those for the tidal flow. The largest change in friction parameters (increase of about 40%) is observed in the North Passage and in the South Passage.

Larger tidal forcing leads to the increase of both tidal elevation and tidal current amplitudes (Fig. 8 panel a and c). Nonetheless, the tidal waves travel slower, because of the larger friction (panel b). For example, the high water at the first branching point ($x = 0$) arrives 11 minutes later during spring tide than during mean tide in the model. When comparing the panel d–f with those of Fig. 5, it appears that the

pattern of horizontal tidal velocity amplitudes does not change from mean tide to spring tide, only amplitudes get larger. The maximum increase is observed at the landward side of the South Passage. River flow is almost unaffected by the larger tidal forcings.

The model is also run for the neap tide (50% lower tidal forcing), which show changes, with respect to mean tide, that are opposite to those for spring tide: friction parameters decrease, tides travel faster, tidal elevation and discharge amplitudes increase.
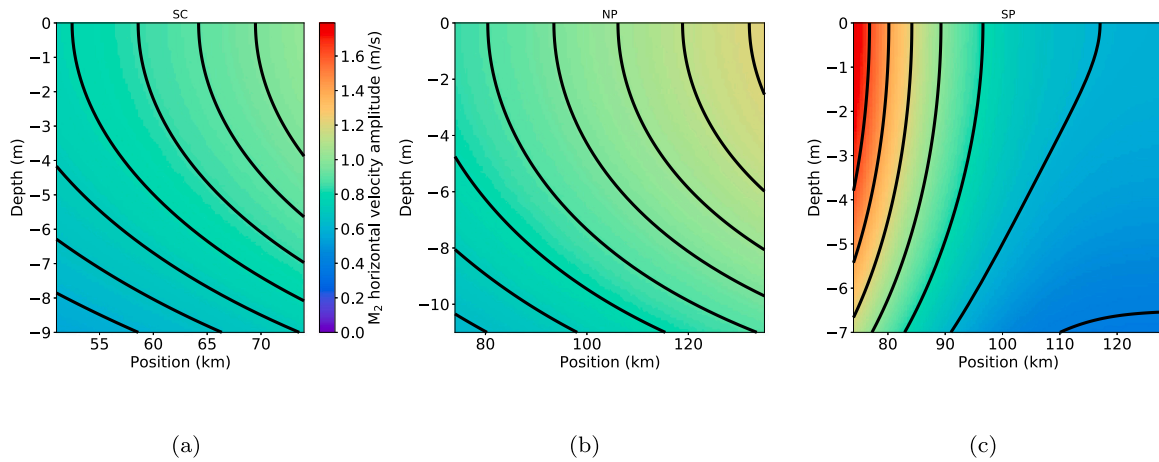
Fig. 5. Spatial structure of horizontal tidal current amplitude in the South Channel (a), the North Passage (b) and the South Passage (c) in the *x-z* plane. Colour is the horizontal tidal velocity amplitude.
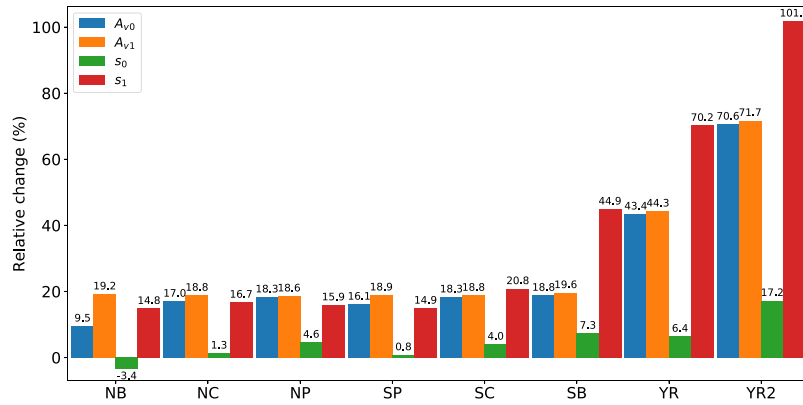

Fig. 6. Relative changes in A_{v0} (blue), A_{v1} (orange), s_0 (green) and s_1 (red) during the wet season with respect to the dry season for the different channels.

SI Fig. 3 shows the sensitivity of variables, as in SI Fig. 2, to values of the tidal forcing that occur during a spring–neap cycle. For larger tidal forcing, tidal elevation amplitudes (panel a) and river set-up (panel c) at the branching point increase. It takes longer for tidal waves to travel to the branching points (panel b). River water transport (panel d) is almost unaffected by the tidal forcing.

3.4. Effects of a shortcut channel (Hengsha Passage)

In this study, the presence of the Hengsha Passage (HP) splits the North Channel (NC) into two channels: the upstream part NC1 and the downstream part NC2. In the HP, positive *x* is defined to be from North to South (from the North Channel at $x = 66$ km to the branching point of the North Passage (NP), the South Passage (SP) and the South Channel (SC) at $x = 74$ km). Since all friction parameters are channel-averaged, splitting the NC affects the averaging, thereby resulting in different values of eddy viscosities and slip parameters. To distinguish the effects of the HP from the effects of splitting the NC, results are first obtained from splitting the NC into two parts. It turns out the effect of splitting the NC is negligible. Then, the HP is added and the results are compared to those obtained from split NC.

It is observed in this model that, in the HP, the tidal current amplitudes are less than 1 m/s, river velocity is small and the river water is transported from the NP to the NC at the rate of about 200 m³/s. The influence of the HP on friction parameters in other channels is shown

in Fig. 9. Friction parameters in the channels connected to the HP are affected most by the HP, the effect is minor; only $1 - 2\%$ and hence negligible within the accuracy of this model.

The effects of the HP on tide, river and river water transport are also mainly in the channels connected to it, i.e., the NC, the NP, the SP and the SC (SI Fig. 4). Due to the presence of the HP, the tidal amplitude at the branching point of the SC, the NP and the SP decreases by a few centimetres (panel a) and tidal amplitude at the junction of the two parts of NC increases. Including the HP, the tidal wave travels slower in the seaward part of the NC (panel b) and faster in the landward part of the NC. These changes lie within the uncertainty margin of the model. Tidal discharge amplitude (panel c) increases in the seaward part of the NC and decreases in the landward part of the NC.

Surface elevations due to the river (panel d) and the river current (panel e) are nearly unaffected by the HP. The changes in the river current imply that the additional river water transport from the SC first enters the HP passages and is subsequently distributed over the two parts of the NC. Moreover, it can be seen from the difference of river water transport (panel f) that the amount of river water transported by the HP mostly goes back to the SC, although the amount is small.
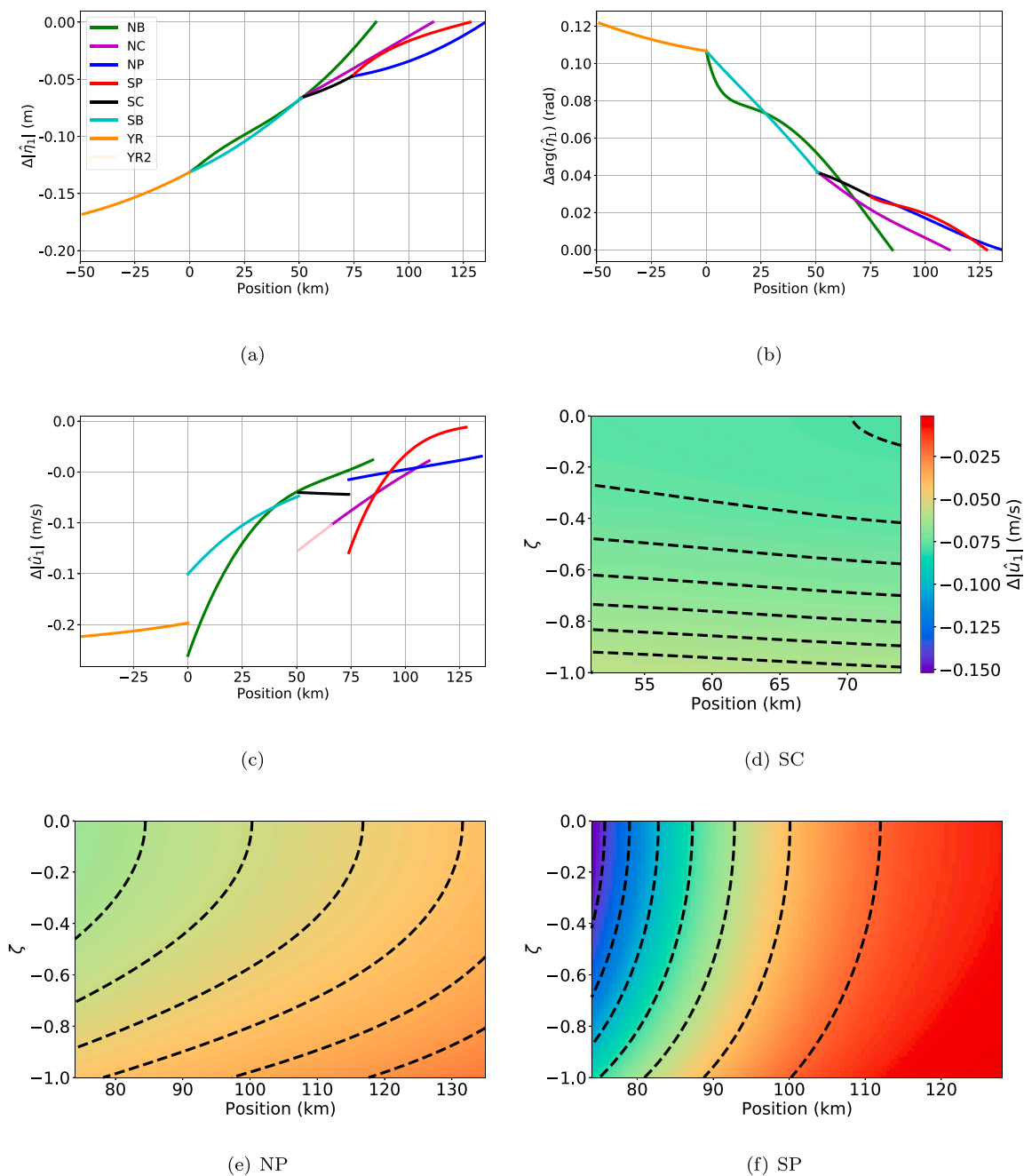
(a)

(b)

(c)

(d) SC

(e) NP

(f) SP

Fig. 7. a. Difference between tidal elevation amplitude during the wet and the dry season versus position in the network. b. As a, but for tidal elevation phase. c. As a, but for tidal discharge amplitude. d. Difference between the horizontal tidal current amplitude in the South Channel (SC) during the wet and the dry season in the x-ζ plane. Colour denotes the difference in the tidal velocity amplitude. e. As d, but for the North Passage (NP). f. As d, but for the South Passage (SP).

3.5. Effects of the Deep Waterway Project (DWP)

The DWP altered the geometric characteristics of the North Passage (NP) in two aspects: the construction of two training walls that significantly reduced the channel convergence and dredging from $7\,\mathrm{m}$ to $11\,\mathrm{m}$ (Jiang et al., 2012).

The effects of the DWP on the friction parameters are mainly in the NP itself (SI Fig. 5). Before the DWP, eddy viscosities for both tide and river in the NP were about 58% smaller than the reference case because eddy viscosities scale with depth. The relative changes in friction parameters in other channels are small.

Tidal elevation amplitudes in all channels were slightly lower than those in the present-day situation (SI Fig. 6a) and the tidal waves travelled slower in most channels (panel b), except for the seaward part of the NP. The upstream amplification of tidal current amplitude was much stronger in the NP (panel c), due to the strong width convergence. Elevation (panel d), velocity (panel e) and the transport (panel f) due to river were similar to those of the reference case. The effects of DWP on the horizontal and vertical structure of tidal current amplitudes are shown in Fig. 10. Panels (a) and (c) are for the South Channel and for the South Passage, in both of which the differences are small. In the NP (panel b), tidal velocity amplitudes in the seaward part significantly increased after the DWP, while in the landward part they decreased. Before the DWP, the near surface tidal velocity amplitude in the NP was more than $0.2\,\mathrm{m/s}$ larger at the branching point and about $0.2\,\mathrm{m/s}$ smaller at the sea.

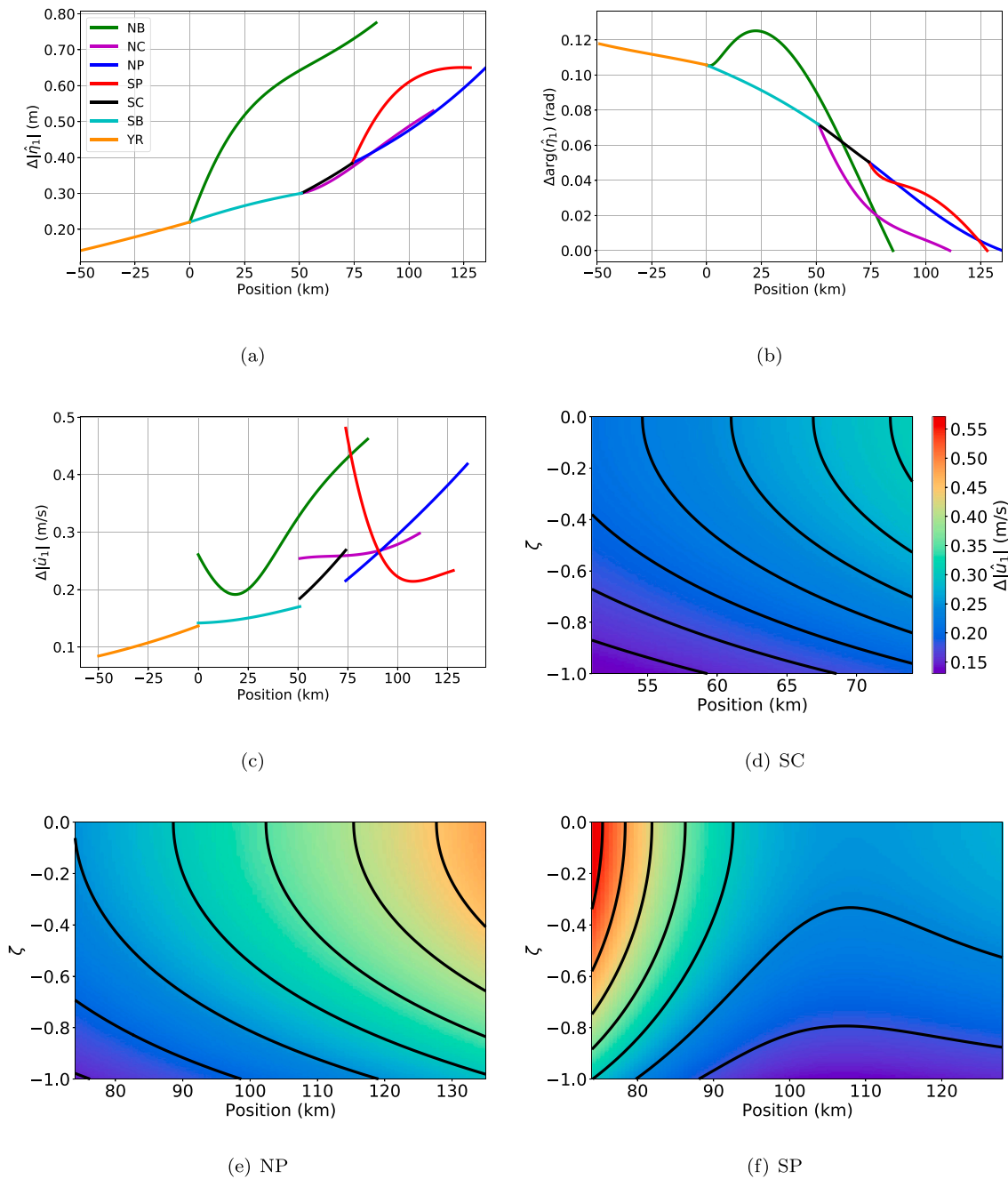(a)

(b)

(c)

(d) SC

(e) NP

(f) SP

Fig. 8. As Fig. 7, but for the difference between spring tide and mean tide.

3.6. Effects of sea level rise

In this study, 2 m seal level rise (SLR) is simplified to a 2 m increase in water depths in all channels. Here, 2 m is the suggested maximum SLR based on the study of Kuang et al. (2014b). Tidal limit moves further upstream due to larger water depth. However, this does not affect the tidal characteristics in the downstream channels. The eddy viscosities for both tide and river increase (SI Fig. 7). The increases in the eddy viscosity for the river flow are slightly larger than that for the tidal flow for all channels with a maximum increase of over 56% in the NB and a minimum increase of about 14% in the NP. The slip parameters for river flow slightly decrease in the NP and the SP and increase in other channels.

With the same tidal forcings, tidal elevation amplitudes within the estuarine network will be enhanced by 2 m SLR (Fig. 11 a) and the amplification is stronger upstream. There is a fair agreement between modelled tidal amplitudes and those obtained with the numerical model of Kuang et al. (2014b) under 2 m SLR. The tidal waves travel faster than those in the reference case (panel b). For example, the high water arrives about 32 minutes earlier at the first branching point $x = 0$. However, the numerical results from Kuang et al. (2014b) predict the advancement of time of high water due to 2 m SLR is about 45 minutes. This difference is mostly likely the consequence of simplified geometry. Changes in tidal current amplitudes are small except for that in the North Branch (NB) (panel c). Due to 2 m SLR, tidal current amplitudes increase in the upstream of the North Branch and the South Branch and decreases in the North Passage are consistent with the
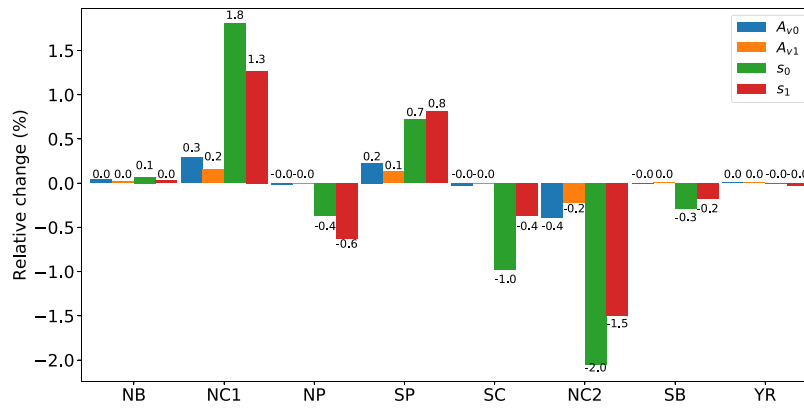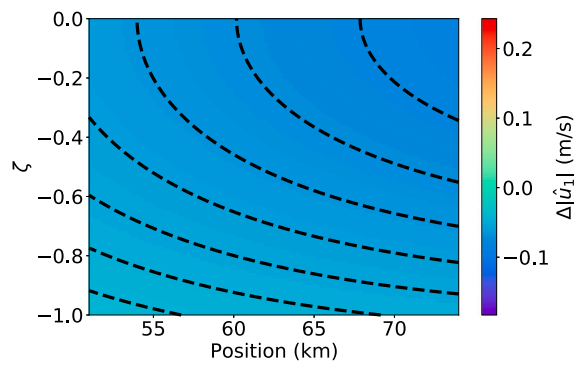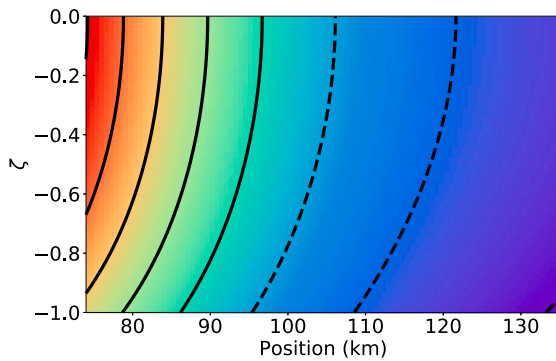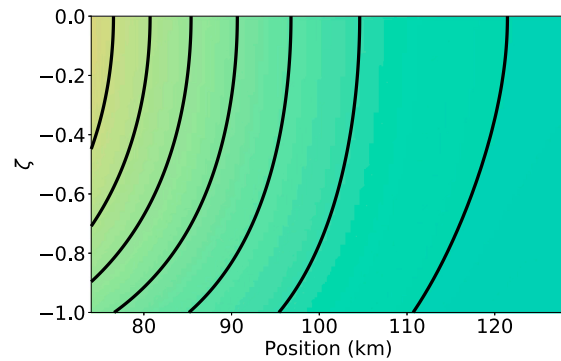
Fig. 9. As Fig. 6, but for the relative changes in friction parameters including the HP with respect to the reference case.

(a) SC

(b) NP

(c) SP

Fig. 10. As Fig. 7 d–f, but for the difference between horizontal tidal velocity amplitudes prior to and after the Deep Waterway Project (DWP).

findings of Kuang et al. (2014b). Surface elevation due to river (panel d) and the river flow velocity (panel e) slightly decrease. The NB and the SP receive a larger fraction of river water, about 100 m^3/s, after SLR compared to the reference case (panel f). Horizontal tidal current amplitudes slightly decreases in the SC, the NP and the SP (Fig. 11), with a maximum decrease of 0.1 m/s at the sea boundary of the SP at the surface. (Fig. 12)

SI Fig. 8 shows variables, as in SI Fig. 2, as continuous functions of imposed sea level rise. As the sea level rises, up to 2 m, the tidal elevation amplitudes increase (panel a) and the river set-ups (panel c)

decrease, tidal waves travel faster (panel b) and river water transport is hardly affected by sea level rise (panel d).

4. Discussion

This section will first summarise the key finds of each experiment and explain the observed changes where necessary. Meanwhile, results will be compared with those reported in other studies. Finally, some limitations of the model will be discussed.
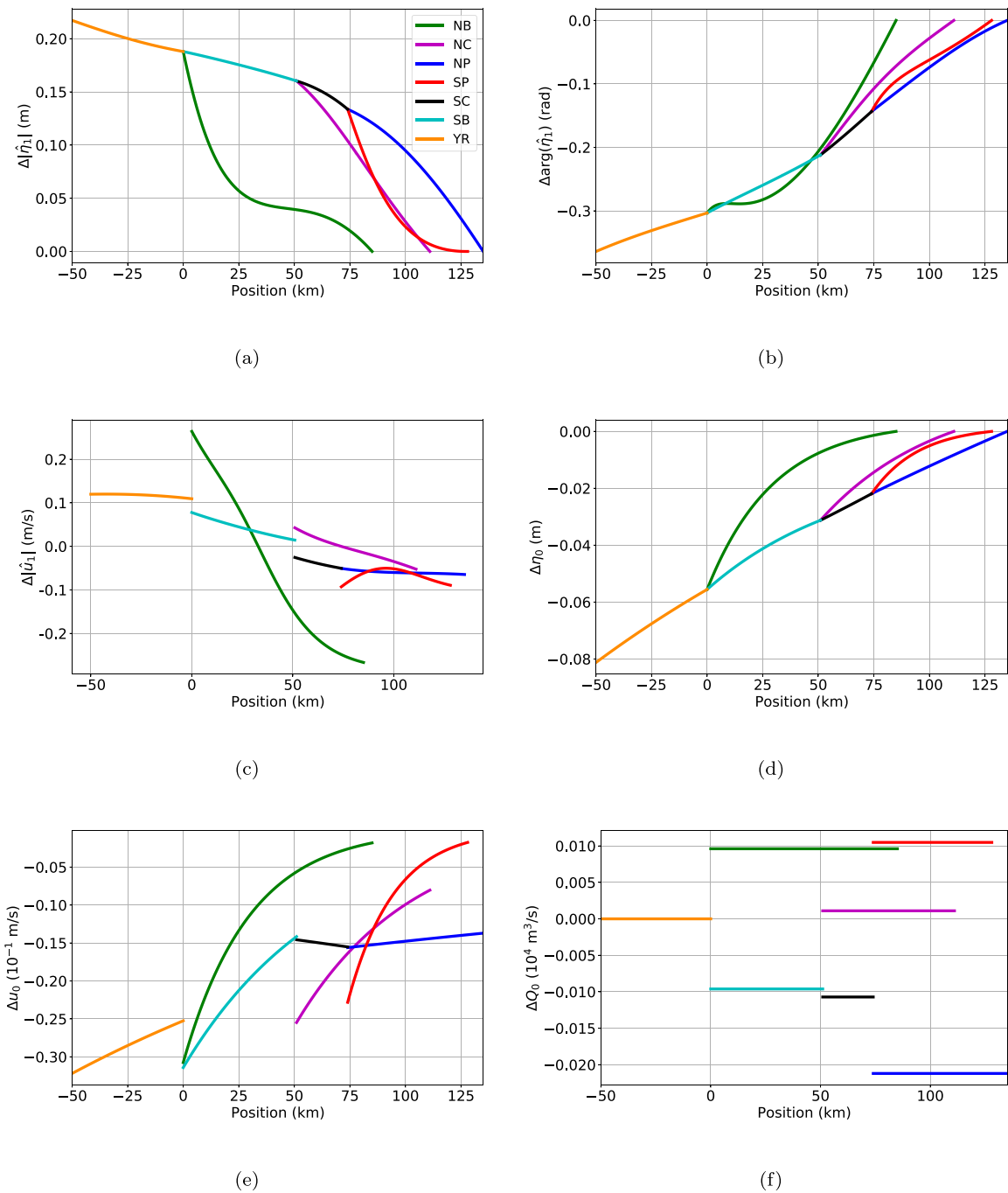
Fig. 11. As Fig. 7, but for the difference between values of variables in the situation for 2 m sea level rise and those in the reference case.

4.1. Key findings

4.1.1. Wet versus dry season

Volumetric river discharge is proportional to the cross-sectionally averaged current, channel width and depth ($Q = UBH$). In our study, B was assumed to be independent of discharge and mean depths in the river channels were adjusted manually according to information provided by Cai et al. (2019). Hence the results are for velocity and its vertical structure. Our results (Fig. 6) reveal that the vertical profiles of the river current are hardly affected by the larger discharge. This is because friction parameters affecting river flow hardly change between

the wet and dry season. However, the eddy viscosities and slip parameters affecting the tide are larger during the wet season due to both enhanced internal stress and bottom stress generated by the tide–river interaction. This can be seen from Eq. (A.7): the contribution of river velocity shear to the internal stress of tidal flow is three times larger than its contribution to the internal stress of the river flow. Due to this increased friction, the tidal wave decays faster and it travels slower when river discharge increases. These findings are consistent with those of earlier studies (e.g. Guo et al., 2015; Cai et al., 2019).

The effect of enhanced tidal decay due to enhanced frictions during the wet season is especially notable in the more upstream branches (Fig. 7a). In the branches close to the sea, such as the NP, the fixed
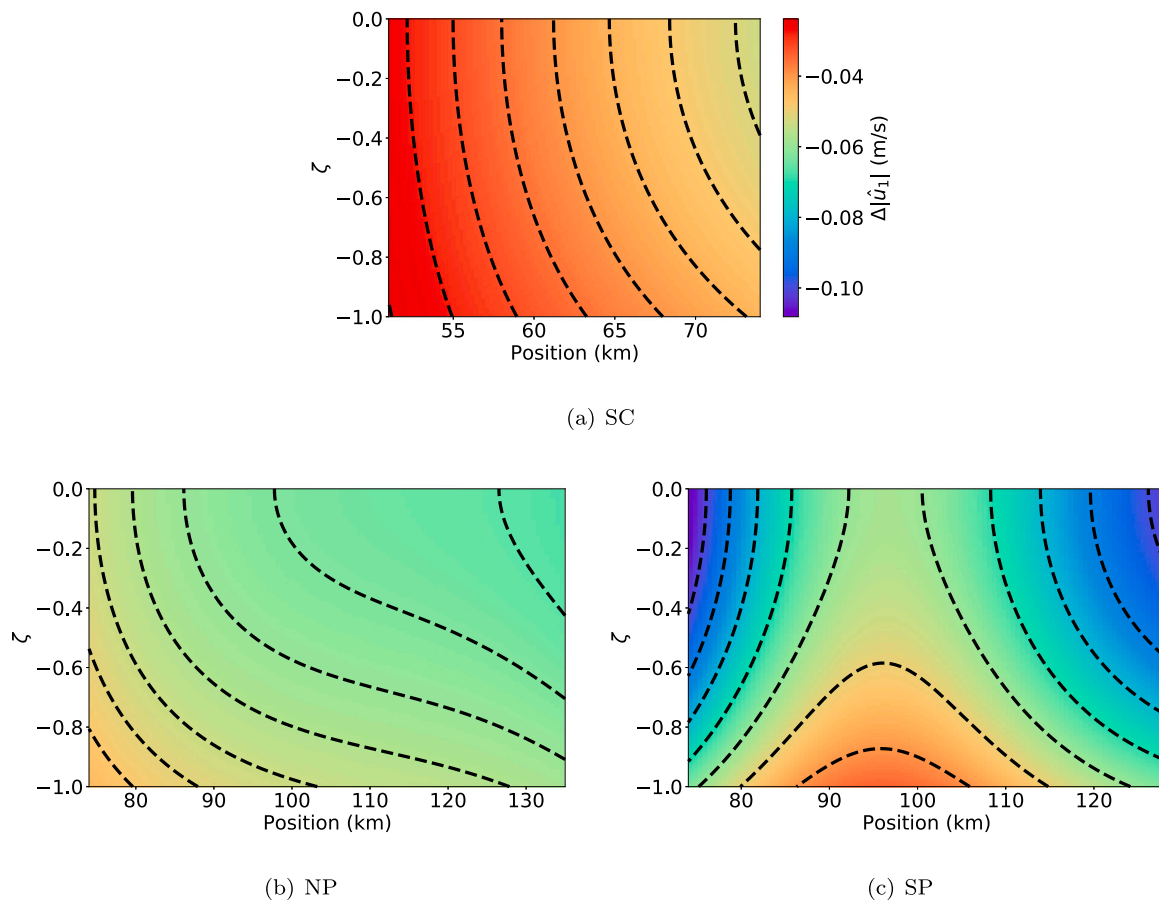
(a) SC

(b) NP

(c) SP

Fig. 12. As Fig. 7d–f, but for the difference between horizontal tidal velocity amplitudes after 2 m sea level rise and those in the reference case (no sea level rise).

boundary condition (tidal amplitude) and enhanced friction lead to an enhanced local pressure gradient, which tends to increase the velocity amplitude (Fig. 7c). The combined effect of enhanced friction and local pressure gradients means that the velocity does not change much in the NP.

Mean energy dissipation in each channel (Eqs. (5) and (11)), averaged over both one tidal cycle and over the entire channel, increases for larger river discharge (SI Fig. 9). This is consistent with earlier findings by Zhu et al. (2016). It turns out that the contribution due to the internal stress is one order of magnitude smaller than that due to the bottom stress.

4.1.2. Spring tide versus mean tide

When tidal forcing increases, the ratio of friction to inertia increases, so tidal waves become more dissipative. Therefore, whether or not the tidal elevation amplitude becomes larger depends on the location. For the Yangtze Estuary, tidal elevation amplitudes increase with larger tidal forcing (Fig. 8a). Larger tidal forcing also causes enhanced tidal velocity shear (Fig. 8d–f), which results in larger eddy viscosities (Eqs. (6)–(7)) and hence larger internal friction. The fact that tidal waves travel slower in the network when tidal forcings are increased is thus caused by the increases in both sources of friction.

4.1.3. The Hengsha Passage (HP)

The overall effects of the Hengsha Passage on tide, river and river water transport are small and local, as was found in Section 3. There is an additional amount of river water that flows from the South Channel (SC) into the HP and flows back to the SC through the upstream part of

North Channel (NC2) (SI Fig. 4f). This explains that the most significant changes in friction parameters are in the NC2 (Fig. 9), i.e., the upstream part of the North Channel.

This model yields the same flow direction as that of Kuang et al. (2014a): water mass is transported from the NP to the NC during maximum flood and from the NC to the NP during the maximum ebb. The tidal current amplitudes in the HP are smaller than those from Kuang et al. (2014a). This is because the configuration of the HP is slightly different in this study: the HP is not only connected to NP, but also the NC, the SP and the SC. This is done to simplify the network configuration; otherwise the NP is split into a downstream part and an upstream part. With this configuration, the tidal elevation amplitudes difference between the two endpoints of the HP, which in general determines the tidal current amplitudes in the HP, is smaller than what is found by Kuang et al. (2014a). Consequently, the tidal current amplitudes in the HP are underestimated.

4.1.4. Effects of the Deep Waterway Project (DWP)

The results for depth-independent variables are similar to those of Alebregtse and de Swart (2016) and are also consistent with data presented in Jiang et al. (2013). Therefore the results are not presented in depth but are included in the SI.

Although the geometrical changes of the DWP are local (larger water depth and less width variation in NP), the intervention affected tides and river water transport in the entire network. Since the DWP involves changes in both depth and width, their effects on depth-independent variables (tidal elevation amplitudes, phases, river set-up, river current and river water transport) are shown separately in SI Fig.

10. The effects of channel deepening and narrowing were comparable in magnitude but opposite and hence compensated each other. This is because their opposite effect on the channel cross-sectional area.

4.1.5. Sea level rise

In this study, sea level rise (SLR) scenario isolates the effect of depth increase only, ignoring some of the other effects of SLR. For example, Kuang et al. (2017) show that when SLR is 2 m, there will be about 0.2 m increase in the tidal forcing amplitudes at the open sea. In this manuscript, effects of the varying tidal forcing amplitudes have been investigated in the spring–neap modulation and therefore boundary conditions are not changed for SLR. It is also assumed that the stratification effect on eddy viscosity remains the same under SLR, and therefore the same calibration parameter as the reference case is used.

Due to a 2 m SLR and under above assumptions, the eddy viscosities for both tide and river increase. This is because the eddy viscosity scales with the water depth (Eq. (6)). Despite the larger friction parameters, the tidal waves travel faster. The reason is that the increased undisturbed water depth leads to an increase in the shallow water wave speed $c = \sqrt{gH}$, the speed that tidal wave travels in the absence of friction. Additionally, a reduction of the set-up induced by river is observed for 2 m SLR (SI Fig. 11). Eq. (16b) shows that the surface gradient is proportional to eddy viscosity coefficient, but inversely proportional to the depth cubed. The latter effect is stronger than the former and therefore the surface gradient decreases. Since the set-up is fixed to be 0 at the sea, smaller surface gradient leads to smaller river set-up. For this reason, the changes in the mean depth inside the estuarine network are smaller than the imposed SLR (SI Fig. 12). Finally, SLR leads to weaker river velocity, because the cross-sections become larger, while the river water transport division in the network is hardly affected.

4.2. Model advantages and limitations

The exploratory nature of this model allows a fast and semi-analytical way to gain fundamental insight into the global tidal motion in networks. It has been used here to better understand the interaction between tidal propagation and friction. Additionally, it includes the distribution of river discharge, which is a contribution to the net water transport. However, idealised nature of the model also imposes some restrictions on the interpretation of the model.

Lateral processes are omitted. These are important in estuaries that are partially to poorly mixed and that have significant lateral depth variations (e.g. Scully et al., 2009). Significant lateral flow has also been observed in the Yangtze Estuary (Li et al., 2019). The length scale being considered in this model is the tidal wavelength. This means that model results are representative for the average motion in width-averaged sense and over length scales of the order of at least 10 km. Smaller details are not resolved. Tidal flats are neglected in this model, which are sinks for along-channel momentum (Hepkema et al., 2018) and have large impact on the dynamics in the inner delta region of the Yangtze Estuary (Zhu et al., 2016).

The effect of density stratification on values of eddy viscosities (Burchard, 2002) is not accounted for. As is shown in e.g. Chen and de Swart (2016), this affects the vertical structure of the tidal current. It may result in a maximum current that does not occur at the surface, which is what is observed in e.g. the North Passage of the Yangtze Estuary (Jiang et al., 2013).

Internally generated overtides are not modelled, which alter the semi-diurnal tidal elevation and usually arise from the nonlinear advection term and friction. Other tidal constituents such as S_2 and diurnal components are not included in the model, but can be added. The model only considers river water transport; it does not yield information about net water transport. The latter also involves net (Stokes) transport by tides, as well as transport due to residual currents induced
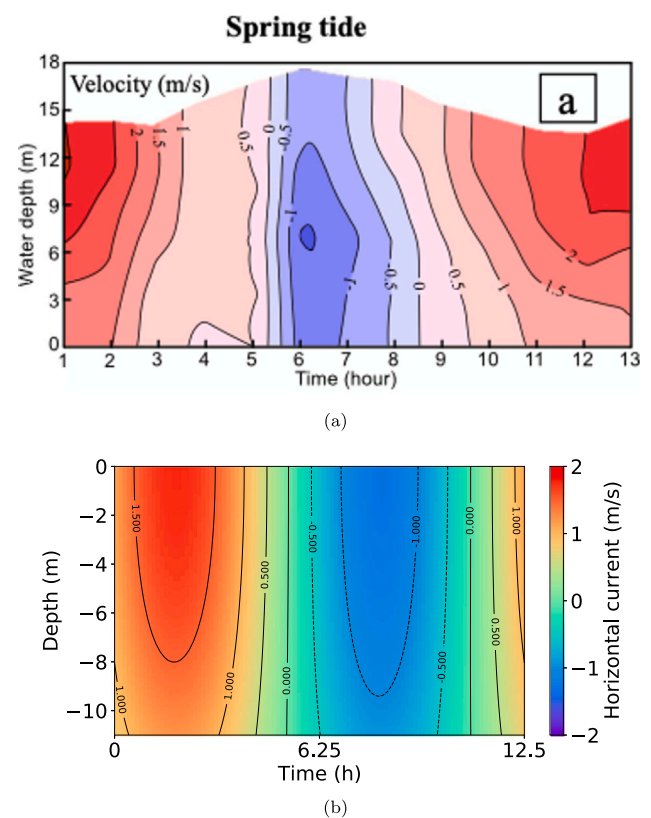
(a)

(b)

Fig. 13. a. Observed vertical structure of the horizontal current near $x = 100$ km in the NP during the wet season for spring tide (Wan and Zhao, 2017). b. Time series reconstructed from the model under the same conditions as of a.

by horizontal density gradients, tidal advection, tidal straining and wind, which are important in estuaries (Geyer and MacCready, 2014; Cheng et al., 2019) and will be considered in a future study.

The time series of the horizontal flow velocity at one location in the North Passage during the wet season for spring tide is constructed from the model and compared to the measurement made by Wan and Zhao (2017) (Fig. 13), which is also comparable to the observation made by Li et al. (2019). Overall, there is a fair agreement between the modelled current vertical structure with that from observation, when taking into account the above mentioned model limitations. First, the maximum flood and ebb currents from our model are smaller than observation. This is because the result from the model is width-averaged. The measurement was made in the middle of the channel and the current near the wall is supposed to be much smaller. Second, the maximum flood current in the middle of the water column near 6 h cannot be reproduced by our model. This is most likely due to the exchange flow, while the only residual flow in our model is river. Third, the second slack tide near $8 - 8.5$ h was not depth uniform. The phase difference at different water depth is mostly likely the consequence of overtides, which is not revolved in the present model.

5. Conclusions

This study focused on the hydrodynamic response of estuarine networks to imposed tidal forcing and river discharge, as well to changes in the response due to changes in forcing (including sea level rise) and geometrical characteristics of the network. For this, a generic, idealised 2DV estuarine network model was developed and applied to the Yangtze Estuary. The model describes primary tides and river water

transport and accounts for river–tide interaction in the turbulence dissipation term. Various local and global modifications were explained via the interaction between eddy viscosity, bottom friction and tidal propagation in the network.

It turns out that the modelled tides and distribution of river water transport in the networks agree fairly well with observations and other model studies, as well as the current vertical structure. The behaviour of tides can be understood in terms of competition between friction and channel width convergence, while the distribution of river water transport is mainly controlled by the geometrical characteristics of each channel.

When river discharge is increased, the tidal wave travels slower and tidal elevations are dampened due to both larger bottom stress and internal stress. River flow is hardly affected by larger discharge; elevation and current due to the river homogeneously change with the prescribed river water discharge.

Varying the amplitude of tidal forcing at the seaward boundaries, that represents the spring–neap modulation, leads to the changes of friction parameters whose values are positively correlated to the tidal forcing amplitude. When tidal forcing amplitude is increased, the tidal wave travels slower due to larger friction. The changes in tidal elevation amplitudes depend on the location, they are enhanced in the downstream part of the Yangtze Estuary. River water transport is nearly unaffected by the variation of tidal forcings.

Results are sensitive to the network geometry. If a connecting channel (Hengsha Passage) is added, changes are mainly local: it reduces the differences in both tidal elevation amplitudes and river set-up in adjacent channels and a net river water transport from the North Passage (NP) to the South Channel (SC) is observed. The effect of the Deep Waterway Project (DWP), a major intervention in which one of the channels (NP) was deepened and straightened (almost no width variations), were global. The effect of deepening was dominant while compensated by the straightening. Noticeable here is the strong increase of tidal currents in the seaward part of NP and a decline in its landward part.

Finally, a 2 m sea level rise results in larger tidal elevation amplitudes, larger phase speed of the tidal waves and reduced river set-up with respect to the undisturbed water depth. River water transport is not sensitive to sea level rise.

Declaration of competing interest

Acknowledgements

Appendix A. Harmonic decomposition of internal and bottom stresses

To estimate the values for friction parameters, the energy dissipation at each harmonic component using the space- and time-dependent turbulence closure will be derived. For clarity, the formulations of eddy viscosity and slip parameter are repeated

$$A_v = l^2 \left| \frac{\partial u}{\partial z} \right|, \quad \text{and} \quad s_f = C_{100}|u_b|. \tag{A.1}$$

Here, l is the mixing length given in Eq. (7), u is the local velocity that contains all harmonic frequencies and u_b is the local velocity at the bottom. The averaged subtidal energy dissipation is

$$D = \overline{A_v \left(\frac{\partial u}{\partial z} \right)^2} = \overline{\tau \frac{\partial u}{\partial z}} \quad \text{and} \quad D_b = \overline{s_f u_b^2} = \overline{\tau_b u_b}, \tag{A.2}$$

where an overline is the averaging over both one tidal cycle and over the channel, defined in the main text (Eq. (5)) and τ and τ_b are the kinematic internal stress and bottom stress respectively,

$$\tau = l^2 \left| \frac{\partial u}{\partial z} \right| \frac{\partial u}{\partial z} \quad \text{and} \quad \tau_b = C_{100}|u_b|u_b. \tag{A.3}$$

Both of them are of the following form

$$f(\boldsymbol{x}, t) = \alpha |g(\boldsymbol{x}, t)| g(\boldsymbol{x}, t), \tag{A.4}$$

where $\boldsymbol{x}$ is the independent variable for space and the coefficient α is required to be time independent. Using the harmonic truncation, the state variable $g \in \left\{ \frac{\partial u}{\partial z}, u_b \right\}$ is written as

$$g = g_0(\boldsymbol{x}) + g_1(\boldsymbol{x}, t) = g_0(\boldsymbol{x}) + \frac{1}{2} \left(\hat{g}_1(\boldsymbol{x}) e^{-i\omega t} + \hat{g}_1(\boldsymbol{x})^* e^{i\omega t} \right), \tag{A.5}$$

where the subscript denotes the harmonic component, a hat implies the complex amplitude and the superscript $(\cdot)^*$ denotes the complex conjugate. Here, g_0 and g_1 are the solutions obtained using constant eddy viscosities $\check{A}_{v0,1}$ and constant slip parameters $\check{s}_{0,1}$. Then the nonlinear function f can be approximated by spectral methods such as using Chebyshev polynomials (Godin, 1999). The procedure is identical to that of Alebregtse and de Swart (2016). Truncate the results after M_2 yields

$$f = \alpha |g_0| g_0 \approx f_0(\boldsymbol{x}) + f_1(\boldsymbol{x}, t)$$

$$= \underbrace{\frac{16\alpha}{15\pi} G \left[1 + \frac{6}{G^2} \left(\frac{1}{3} g_0^2 + \frac{1}{2} |\hat{g}_1|^2 \right) \right] g_0}_{f_0}$$

$$+ \underbrace{\frac{16\alpha}{15\pi} G \left[1 + \frac{6}{G^2} \left(g_0^2 + \frac{1}{4} |\hat{g}_1|^2 \right) \right] \text{Re}\{ \hat{g}_1 e^{-i\omega t} \}}_{f_1}. \tag{A.6}$$

where $G = |g_0| + |\hat{g}_1|$ is the scale of g. Therefore, the M_0 (residual) and M_2 components of the local internal stress are

$$\tau_0 = \frac{16 l^2}{15\pi} G_I \left[1 + \frac{6}{G_I^2} \left(\frac{1}{3} \left(\frac{\partial u_0}{\partial z} \right)^2 + \frac{1}{2} \left| \frac{\partial \hat{u}_1}{\partial z} \right|^2 \right) \right] \frac{\partial u_0}{\partial z}, \tag{A.7}$$

$$\tau_1 = \text{Re}\{ \hat{\tau}_1 e^{-i\omega t} \}$$

$$= \text{Re} \left\{ \frac{16 l^2}{15\pi} G_I \left[1 + \frac{6}{G_I^2} \left(\left(\frac{\partial u_0}{\partial z} \right)^2 + \frac{1}{4} \left| \frac{\partial \hat{u}_1}{\partial z} \right|^2 \right) \right] \frac{\partial \hat{u}_1}{\partial z} e^{-i\omega t} \right\}, \tag{A.8}$$

where $G_I = \left| \frac{\partial u_0}{\partial z} \right| + \left| \frac{\partial \hat{u}_1}{\partial z} \right|$ is the magnitude of the local velocity shear. Similarly, the M_0 and M_2 components of the local bottom stress are

$$\tau_{b0} = \frac{16 C_{100}}{15\pi} G_b \left[1 + \frac{6}{G_b^2} \left(\frac{1}{3} u_{b0}^2 + \frac{1}{2} |\hat{u}_{b1}|^2 \right) \right] u_{b0}, \tag{A.9}$$

$$\tau_{b1} = \text{Re}\{ \hat{\tau}_{b1} e^{-i\omega t} \} = \text{Re} \left\{ \frac{16 C_{100}}{15\pi} G_b \left[1 + \frac{6}{G_b^2} \left(u_{b0}^2 + \frac{1}{4} |\hat{u}_{b1}|^2 \right) \right] \hat{u}_{b1} e^{-i\omega t} \right\}, \tag{A.10}$$

where $G_b = |u_{b0}| + |\hat{u}_{b1}|$ is the magnitude of the local bottom velocity.

Next, applying harmonic truncation Eq. (A.5) to the subtidal energy dissipation and using the results of decomposed stresses yields

$$D = \overline{(\tau_0 + \tau_1) \left(\frac{\partial u_0}{\partial z} + \frac{\partial u_1}{\partial z} \right)} = \underbrace{\overline{\tau_0 \frac{\partial u_0}{\partial z}}}_{D_0} + \underbrace{\overline{\tau_1 \frac{\partial u_1}{\partial z}}}_{D_1}, \tag{A.11}$$

$$D_b = \overline{(\tau_{b0} + \tau_{b1})(u_{b0} + u_{b1})} = \underbrace{\overline{\tau_{b0}u_{b0}}}_{D_{b0}} + \underbrace{\overline{\tau_{b1}u_{b1}}}_{D_{b1}}. \tag{A.12}$$

Here, the cross terms vanish due to the averaging over one tidal cycle. The subtidal energy dissipation due to both internal stress and bottom stress contain two parts: the contribution of M_0 river flow (D_0 and D_{b0}) and M_2 tidal flow (D_1 and D_{b1}). These dissipation contributions are assumed to be the same as when using constant friction parameters $\check{A}_{v0,1}$ and $\check{s}_{0,1}$, i.e.,

$$D_n = \check{D}_n \quad \text{and} \quad D_{bn} = \check{D}_{bn}, \tag{A.13}$$

where $\check{D}_n$ and $\check{D}_{bn}$ are given in Eqs. (5) and (11). These criteria give the expressions for constant friction parameters, the results are

$$\check{A}_{v0} = \frac{\overline{\tau_0 \frac{\partial u_0}{\partial z}}}{\left(\frac{\partial u_0}{\partial z}\right)^2}, \quad \check{A}_{v1} = \frac{\mathrm{Re}\left\{\overline{\hat{\tau}_1^* \frac{\partial \hat{u}_1}{\partial z}}\right\}}{\left|\frac{\partial \hat{u}_1}{\partial z}\right|^2}, \tag{A.14}$$

$$\check{s}_{f0} = \frac{\overline{\tau_{b0}u_{b0}}}{\overline{u_{b0}^2}}, \quad \check{s}_{f1} = \frac{\mathrm{Re}\left\{\overline{\hat{\tau}_1^* \hat{u}_{b1}}\right\}}{\left|\hat{u}_{b1}^2\right|}. \tag{A.15}$$

Appendix B. Solutions

B.1. Solutions for river flow

The river flow is governed by Eqs. (2) of the main text, assuming $n = 0$. To obtain the solutions, integrate the momentum equation for river flow from some depth $z' = z$ to the linearised free surface $z' = 0$ and apply the boundary condition yielding

$$0 = gz\frac{\partial \eta_0}{\partial x} - \check{A}_{v0}\frac{\partial u_0}{\partial z}. \tag{B.1}$$

Integrate again from the bottom $z' = -H$ to some depth z, which gives

$$u_0 = \frac{(z^2 - H^2)}{2\check{A}_{v0}}g\frac{\partial \eta_0}{\partial x} + u_0|_{z=-H}. \tag{B.2}$$

The slip condition at the bottom implies

$$u_0|_{z=-H} = \frac{\check{A}_{v0}}{\check{s}_{f0}}\frac{\partial u_0}{\partial z}\bigg|_{z=-H} = -\frac{gH}{\check{s}_{f0}}\frac{\partial \eta_0}{\partial x}. \tag{B.3}$$

Hence

$$u_0 = \frac{gH^2}{\check{A}_{v0}}\left[\frac{\left(\frac{z}{H}\right)^2 - 1}{2} - \frac{\check{A}_{v0}}{H\check{s}_{f0}}\right]\frac{\partial \eta_0}{\partial x}. \tag{B.4}$$

Integration of continuity equation and application of the boundary conditions at the bottom and surface gives Eq. (15) in the main text. Application of boundary condition at the river head implies

$$\frac{\partial \eta_0}{\partial x} = -\frac{Q\check{A}_{v0}}{gb(x)H^3}\frac{1}{\frac{1}{3} + \frac{\check{A}_{v0}}{H\check{s}_{f0}}}. \tag{B.5}$$

Eqs. (B.4)–(B.5) are Eqs. (16) in the main text. Note that the vertical velocity is everywhere zero.

B.2. Solutions for tidal flow

Tidal flow can be solved by substituting non-transient periodic trial solutions

$$(u_1, w_1, \eta_1) = \mathrm{Re}\left\{(\hat{u}_1, \hat{w}_1, \hat{\eta}_1)\,e^{-i\omega t}\right\} \tag{B.6}$$

into the governing equations and boundary conditions (Eqs. (2)–(4)) of the main text for $n = 1$:

$$-i\omega\hat{u}_1 = -g\frac{d\hat{\eta}_1}{dx} + \check{A}_{v1}\frac{\partial^2 \hat{u}_1}{\partial z^2}, \tag{B.7a}$$

$$0 = \frac{\partial \hat{u}_1}{\partial x} + \frac{\partial \hat{w}_1}{\partial z} + \frac{1}{l_b}\hat{u}_1, \tag{B.7b}$$

$$\check{A}_{v1}\frac{\partial \hat{u}_1}{\partial z} = 0, \qquad \hat{w}_1 = -i\omega\hat{\eta}_1 \qquad \text{at} \quad z = 0, \tag{B.7c}$$

$$\check{A}_{v1}\frac{\partial \hat{u}_1}{\partial z} = \check{s}_{f1}\hat{u}_1, \quad \hat{w}_1 = 0 \qquad \text{at} \quad z = -H. \tag{B.7d}$$

The general solution of Eq. (B.7a) is

$$\hat{u}_1(x,z) = A_1(x)e^{\gamma z} + A_2(x)e^{-\gamma z} - \frac{ig}{\omega}\frac{d\hat{\eta}_1}{dx}, \tag{B.8}$$

where $\gamma = \sqrt{-\frac{i\omega}{\check{A}_{v1}}}$. The first boundary condition in Eq. (B.7c) gives

$$\hat{u}_1(x,z) = A(x)\cosh(\gamma z) - \frac{ig}{\omega}\frac{d\hat{\eta}_1}{dx}. \tag{B.9}$$

Finally, apply the partial slip condition at the bottom $z = -H$ to obtain

$$\hat{u}_1(x,z) = \frac{ig}{\omega}[\beta\cosh(\gamma z) - 1]\frac{d\hat{\eta}_1}{dx}. \tag{B.10}$$

where β is defined in the main text. Next, substitute of Eq. (B.10) into the continuity (B.7b), integrate over depth and use of the boundary condition $\hat{w}_1 = -i\omega\hat{\eta}_1$ at $z = 0$ yields

$$\hat{w}_1(x,z) = -\frac{ig}{\omega}\left[\frac{\beta}{\gamma}\sinh(\gamma z) - z\right]\left(\frac{d^2\hat{\eta}_1}{dx^2} + \frac{1}{l_b}\frac{d\hat{\eta}_1}{dx}\right) - i\omega\hat{\eta}_1. \tag{B.11}$$

The boundary condition at the bottom ($w_1 = 0$ at $z = -H$) implies that the surface amplitude should obey the differential equation

$$\frac{g}{\omega}\left[\frac{\beta}{\gamma}\sinh(\gamma H) - H\right]\left(\frac{d^2\hat{\eta}_1}{dx^2} + \frac{1}{l_b}\frac{d\hat{\eta}_1}{dx}\right) - \omega\hat{\eta}_1 = 0. \tag{B.12}$$

Its general solution is

$$\hat{\eta}_1 = C_1 e^{k_1 x} + C_2 e^{k_2 x}, \tag{B.13}$$

where

$$k_{1,2} = -\frac{1}{2l_b} \pm \sqrt{\left(\frac{1}{2l_b}\right)^2 + \frac{\gamma\omega^2}{g[\beta\sinh(\gamma H) - \gamma H]}} \tag{B.14}$$

are the two complex wave number. This expression is equivalent to Eq. (18c) by factoring out $-\frac{1}{2l_b}$ in the complex wave numbers, which describe the exponential decay of the tidal wave due to the variation of channel width.

```
┌─────────────────────────────────┐
│   Initial guess for con-        │
│   stant friction parameters     │
└─────────────────────────────────┘
                 ↓
┌─────────────────────────────────┐
│   Solution to river and tide    │
│   (Eq. (16), (18)) with un-     │
│   known integration constants   │
└─────────────────────────────────┘
                 ↓
┌─────────────────────────────────┐
│   Determine integration con-    │
│   stants by boundary and        │
│   matching conditions (Eq. (4)) │
└─────────────────────────────────┘
                 ↓
┌─────────────────────────────────┐
│   Estimate energy dissipa-      │
│   tion with constant friction   │
│   parameters (Eq. (5), (11))    │
└─────────────────────────────────┘
                 ↓
┌─────────────────────────────────┐
│   Compute dissipation using a   │
│   space- and time-dependent     │
│   turbulence closure            │
│   (Eq. (A.11), (A.12))          │
└─────────────────────────────────┘
                 ↓
          ◇ Is dissipation the same? ◇
           │ No (left)      │ Yes (down)

┌─────────────────────────────────┐
│   Update constant friction pa-  │
│   rameters (Eq. (10), (14))     │
└─────────────────────────────────┘

┌─────────────────────────────────┐
│             stop                │
└─────────────────────────────────┘
```

Appendix C. Solution procedure

Appendix D. Supplementary data

Supplementary material related to this article can be found online at https://doi.org/10.1016/j.csr.2021.104476.

References

Alebregtse, N., de Swart, H.E., 2016. Effect of river discharge and geometry on tides and net water transport in an estuarine network, an idealized model applied to the Yangtze Estuary. Cont. Shelf Res. 123, 29–49. http://dx.doi.org/10.1016/j.csr.2016.03.028.

Bradshaw, P., 1974. Possible origin of Prandtl's mixing-length theory. Nature 249 (5453), 135–136. http://dx.doi.org/10.1038/249135b0.

Burchard, H., 2002. Applied Turbulence Modelling in Marine Waters. Springer-Verlag Berlin Heidelberg, http://dx.doi.org/10.1007/3-540-45419-5.

Buschman, F.A., Hoitink, A.J.F., van der Vegt, M., Hoekstra, P., 2010. Subtidal flow division at a shallow tidal junction. Water Resour. Res. 46 (12), http://dx.doi.org/10.1029/2010WR009266.

Cai, H., Savenije, H.H.G., Garel, E., Zhang, X., Guo, L., Zhang, M., Liu, F., Yang, Q., 2019. Seasonal behaviour of tidal damping and residual water level slope in the Yangtze River estuary: identifying the critical position and river discharge for maximum tidal damping. Hydrol. Earth Syst. Sci. 23 (6), 2779–2794. http://dx.doi.org/10.5194/hess-23-2779-2019.

Chen, W., de Swart, H.E., 2016. Dynamic links between shape of the eddy viscosity profile and the vertical structure of tidal current amplitude in bays and estuaries. Ocean Dyn. 66 (3), 299–312. http://dx.doi.org/10.1007/s10236-015-0919-6.

Cheng, H., Chen, J., Chen, Z., Ruan, R., Xu, G., Zeng, G., Zhu, J., Dai, Z., Chen, X., Gu, S., Zhang, X., Wang, H., 2018. Mapping sea level rise behavior in an estuarine delta system: A case study along the Shanghai coast. Engineering 4 (1), 156–163. http://dx.doi.org/10.1016/j.eng.2018.02.002.

Cheng, P., Mao, J., Yu, F., Chen, N., Wang, A., Xu, F., 2019. A numerical study of residual flow induced by eddy viscosity-shear covariance in a tidally energetic estuary. Estuar. Coast. Shelf Sci. 230, 106446. http://dx.doi.org/10.1016/j.ecss.2019.106446.

Chernetsky, A., Schuttelaars, H., Talke, S., 2010. The effect of tidal asymmetry and temporal settling lag on sediment trapping in tidal estuaries. Ocean Dyn. 60, 1219–1241. http://dx.doi.org/10.1007/s10236-010-0329-8.

Cloern, J.E., Abreu, P.C., Carstensen, J., Chauvaud, L., Elmgren, R., Grall, J., Greening, H., Johansson, J.O.R., Kahru, M., Sherwood, E.T., Xu, J., Yin, K., 2016. Human activities and climate variability drive fast-paced change across the world's estuarine–coastal ecosystems. Global Change Biol. 22 (2), 513–529. http://dx.doi.org/10.1111/gcb.13059.

Dijkstra, Y.M., Brouwer, R.L., Schuttelaars, H.M., Schramkowski, G.P., 2017. The iFlow modelling framework v2.4: a modular idealized process-based model for flow and transport in estuaries. Geosci. Model Dev. 10 (7), 2691–2713. http://dx.doi.org/10.5194/gmd-10-2691-2017.

Dijkstra, Y.M., Schuttelaars, H.M., Schramkowski, G.P., Brouwer, R.L., 2019. Modeling the transition to high sediment concentrations as a response to channel deepening in the Ems river estuary. J. Geophys. Res.: Oceans 124 (3), 1578–1594. http://dx.doi.org/10.1029/2018JC014367.

Friedrichs, C.T., 2010. Barotropic tides in channelized estuaries. In: Valle-Levinson, A. (Ed.), Contemporary Issues in Estuarine Physics. Cambridge University Press, pp. 27–61. http://dx.doi.org/10.1017/CBO9780511676567.004.

Friedrichs, C.T., Aubrey, D.G., 1988. Non-linear tidal distortion in shallow well-mixed estuaries: a synthesis. Estuar. Coast. Shelf Sci. 27 (5), 521–545. http://dx.doi.org/10.1016/0272-7714(88)90082-0.

Friedrichs, C.T., Aubrey, D.G., 1994. Tidal propagation in strongly convergent channels. J. Geophys. Res.: Oceans 99 (C2), 3321–3336. http://dx.doi.org/10.1029/93JC03219.

Geyer, W.R., MacCready, P., 2014. The estuarine circulation. Annu. Rev. Fluid Mech. 46 (1), 175–197. http://dx.doi.org/10.1146/annurev-fluid-010313-141302.

Godin, G., 1991. Compact approximations to the bottom friction term, for the study of tides propagating in channels. Cont. Shelf Res. 11 (7), 579–589. http://dx.doi.org/10.1016/0278-4343(91)90013-V.

Godin, G., 1999. The propagation of tides up rivers with special considerations on the upper Saint Lawrence River. Estuar. Coast. Shelf Sci. 48 (3), 307–324. http://dx.doi.org/10.1006/ecss.1998.0422.

Guo, L., van der Wegen, M., Jay, D.A., Matte, P., Wang, Z.B., Roelvink, D., He, Q., 2015. River-tide dynamics: Exploration of nonstationary and nonlinear tidal behavior in the Yangtze River estuary. J. Geophys. Res.: Oceans 120 (5), 3499–3521. http://dx.doi.org/10.1002/2014JC010491.

Hepkema, T.M., de Swart, H.E., Zagaris, A., Duran-Matute, M., 2018. Sensitivity of tidal characteristics in double inlet systems to momentum dissipation on tidal flats: a perturbation analysis. Ocean Dyn. 68 (4), 439–455. http://dx.doi.org/10.1007/s10236-018-1142-z.

Hill, A.E., Souza, A.J., 2006. Tidal dynamics in channels: 2. Complex channel networks. J. Geophys. Res.: Oceans 111 (C11), http://dx.doi.org/10.1029/2006JC003670.

Ianniello, J.P., 1977. Tidally induced residual currents in estuaries of constant breadth and depth. J. Mar. Res. 35, 755–786.

Ianniello, J.P., 1979. Tidally induced residual currents in estuaries of variable breadth and depth. J. Phys. Oceanogr. 9 (5), 962–974. http://dx.doi.org/10.1175/1520-0485(1979)009<0962:TIRCIE>2.0.CO;2.

Jiang, C., Li, J., de Swart, H.E., 2012. Effects of navigational works on morphological changes in the bar area of the Yangtze Estuary. Geomorphology 139–140, 205–219. http://dx.doi.org/10.1016/j.geomorph.2011.10.020.

Jiang, C., de Swart, H., Li, J., Liu, G., 2013. Mechanisms of along-channel sediment transport in the North Passage of the Yangtze Estuary and their response to large-scale interventions. Ocean Dyn. 63, http://dx.doi.org/10.1007/s10236-013-0594-4.

Kuang, C., Chen, W., Gu, J., He, L., 2014a. Comprehensive analysis on the sediment siltation in the upper reach of the deepwater navigation channel in the Yangtze Estuary. J. Hydrodyn. 26 (2), 299–308. http://dx.doi.org/10.1016/S1001-6058(14)60033-0.

Kuang, C., Chen, W., Gu, J., Zhu, D.Z., He, L., Huang, H., 2014b. Numerical assessment of the impacts of potential future sea level rise on hydrodynamics of the Yangtze River Estuary, China. J. Coast. Res. 30 (3), 586–597. http://dx.doi.org/10.2112/JCOASTRES-D-13-00149.1.

Kuang, C., Liang, H., Mao, X., Karney, B., Gu, J., Huang, H., Chen, W., Song, H., 2017. Influence of potential future sea-level rise on tides in the China sea. J. Coast. Res. 33 (1), 105–117. http://dx.doi.org/10.2112/JCOASTRES-D-16-00057.1.

Kundu, P.K., Cohen, I.M., Dowling, D.R., 2016. In: Kundu, P.K., Cohen, I.M., Dowling, D.R. (Eds.), Fluid Mechanics, sixth ed. Academic Press, Boston, pp. 666–668.

Lanzoni, S., Seminara, G., 1998. On tide propagation in convergent estuaries. J. Geophys. Res.: Oceans 103 (C13), 30793–30812. http://dx.doi.org/10.1029/1998JC900015.

Li, L., He, Z., Xia, Y., Dou, X., 2018. Dynamics of sediment transport and stratification in Changjiang River Estuary, China. Estuar. Coast. Shelf Sci. 213, 1–17. http://dx.doi.org/10.1016/j.ecss.2018.08.002.

Li, Z., Jia, J., Wu, Y., Zong, H., Zhang, G., Wang, Y.P., Yang, Y., Zhou, L., Gao, S., 2019. Vertical distributions of suspended sediment concentrations in the turbidity maximum zone of the periodically and partially stratified Changjiang Estuary. Estuar. Coasts 42 (6), 1475–1490. http://dx.doi.org/10.1007/s12237-019-00605-2.

Lorentz, H.A., 1926. Verslag van de Staatscommissie Zuiderzee. Algemeene Landsdrukkerij, 's Gravenhage, (in Dutch).

Lu, S., Tong, C., Lee, D.-Y., Zheng, J., Shen, J., Zhang, W., Yan, Y., 2015. Propagation of tidal waves up in Yangtze Estuary during the dry season. J. Geophys. Res.: Oceans 120 (9), 6445–6473. http://dx.doi.org/10.1002/2014JC010414.

Maas, L., van Haren, J., 1987. Observations on the vertical structure of tidal and inertial currents in the central North Sea. J. Mar. Res. 45, 293–318. http://dx.doi.org/10.1357/002224087788401106.

National Marine Data and Information Service, 2013. Tide Tables 2014, Vol. 2. China Ocean Press, (in Chinese).

Ridderinkhof, W., de Swart, H.E., van der Vegt, M., Alebregtse, N.C., Hoekstra, P., 2014. Geometry of tidal inlet systems: A key factor for the net sediment transport in tidal inlets. J. Geophys. Res.: Oceans 119 (10), 6988–7006. http://dx.doi.org/10.1002/2014JC010226.

Sassi, M.G., Hoitink, A.J.F., de Brye, B., Vermeulen, B., Deleersnijder, E., 2011. Tidal impact on the division of river discharge over distributary channels in the Mahakam Delta. Ocean Dyn. 61 (12), 2211–2228. http://dx.doi.org/10.1007/s10236-011-0473-9.

Schramkowski, G., de Swart, H., 2002. Morphodynamic equilibrium in straight tidal channels: Combined effects of the Coriolis force and external overtides. J. Geophys. Res.: Oceans 107 (C12), 20–1–20–17. http://dx.doi.org/10.1029/2000JC000693.

Scully, M.E., Geyer, W.R., Lerczak, J.A., 2009. The influence of lateral advection on the residual estuarine circulation: A numerical modeling study of the Hudson River Estuary. J. Phys. Oceanogr. 39 (1), 107–124. http://dx.doi.org/10.1175/2008JPO3952.1.

Shao, Y., Shen, X., Maa, J.P.-Y., Shen, J., 2017. Simulating high ebb currents in the North Passage of the Yangtze Estuary using a vertical 1-D model. Estuar. Coast. Shelf Sci. 196, 399–410. http://dx.doi.org/10.1016/j.ecss.2017.08.001.

Soulsby, R., 1997. Dynamics of Marine Sands. a Manual for Practical Applications. Thomas Telford, London.

Souza, A.J., 2013. On the use of the Stokes number to explain frictional tidal dynamics and water column structure in shelf seas. Ocean Sci. 9 (2), 391–398. http://dx.doi.org/10.5194/os-9-391-2013.

Talke, S.A., Jay, D.A., 2020. Changing tides: The role of natural and anthropogenic factors. Annu. Rev. Mar. Sci. 12 (1), 121–151. http://dx.doi.org/10.1146/annurev-marine-010419-010727.

Valle-Levinson, A., Wong, K.-C., Lwiza, K.M.M., 2000. Fortnightly variability in the transverse dynamics of a coastal plain estuary. J. Geophys. Res.: Oceans 105 (C2), 3413–3424. http://dx.doi.org/10.1029/1999JC900307.

Wan, Y., Zhao, D., 2017. Observation of saltwater intrusion and ETM dynamics in a stably stratified estuary: the Yangtze Estuary, China. Environ. Monit. Assess. 189 (2), 89. http://dx.doi.org/10.1007/s10661-017-5797-6.

Winterwerp, J.C., Erftemeijer, P.L.A., Suryadiputra, N., van Eijk, P., Zhang, L., 2013. Defining eco-morphodynamic requirements for rehabilitating eroding mangrove-mud coasts. Wetlands 33 (3), 515–526. http://dx.doi.org/10.1007/s13157-013-0409-x.

Yang, Z., Cheng, H., Li, J., 2015. Nonlinear advection, Coriolis force, and frictional influence in the South Channel of the Yangtze Estuary, China. Sci. China Earth Sci. 58 (3), 429–435. http://dx.doi.org/10.1007/s11430-014-4946-9.

Zhang, E.F., Savenije, H.H.G., Chen, S.L., Mao, X.H., 2012. An analytical solution for tidal propagation in the Yangtze Estuary, China. Hydrol. Earth Syst. Sci. 16 (9), 3327–3339. http://dx.doi.org/10.5194/hess-16-3327-2012.

Zhang, M., Townend, I., Zhou, Y., Cai, H., 2016. Seasonal variation of river and tide energy in the Yangtze Estuary, China. Earth Surf. Process. Landforms 41 (1), 98–116. http://dx.doi.org/10.1002/esp.3790.

Zhu, L., He, Q., Shen, J., Wang, Y., 2016. The influence of human activities on morphodynamics and alteration of sediment source and sink in the Changjiang Estuary. Geomorphology 273, 52–62. http://dx.doi.org/10.1016/j.geomorph.2016.07.025.

Zhu, J., Wu, H., Li, L., Qiu, C., 2018. Saltwater intrusion in the Changjiang Estuary. In: Liang, X.S., Zhang, Y. (Eds.), Coastal Environment, Disaster, and Infrastructure. IntechOpen, pp. 49–73. http://dx.doi.org/10.5772/intechopen.80903.

Zimmerman, J., 1982. On the Lorentz linearization of a quadratically damped forced oscillator. Phys. Lett. A 89 (3), 123–124. http://dx.doi.org/10.1016/0375-9601(82)90871-4.